# Ultra-efficient decontamination via functionalized reactive electrochemical membrane for peroxymonosulfate activation: High water flux with extremely low energy consumption

Jiana Jing [a,b,c], Huizhong Wu [a,b,c], Jinxin Xie [a,b,c], Xuechun Wang [a,b,c], Minghua Zhou [a,b,c,*]

[a] *Key Laboratory of Pollution Process and Environmental Criteria, Ministry of Education, College of Environmental Science and Engineering, Nankai University, Tianjin 300350, China*
[b] *Tianjin Key Laboratory of Environmental Technology for Complex Trans-Media Pollution, College of Environmental Science and Engineering, Nankai University, Tianjin 300350, China*
[c] *Tianjin Advanced Water Treatment Technology International Joint Research Center, College of Environmental Science and Engineering, Nankai University, Tianjin 300350, China*

## ARTICLE INFO

## ABSTRACT

A perovskite LaCoO$_3$ functionalized Ti$_4$O$_7$ reactive electrochemical membrane (REM) was developed for electro-enhanced peroxymonosulfate (PMS) activation (E-REM-PMS), addressing limitations in wastewater treatment efficiency, reusability, and interference resistance. It achieved 100% carbamazepine (CBZ) removal at a rate constant of 39.69 min$^{-1}$, 233 and 23 times of electro-REM (E-REM) system without PMS and REM-PMS system without electricity. *In-situ* Fourier transform infrared spectroscopy (FTIR) highlighted the promotion of electro-activation on PMS, while density functional theory (DFT) calculations elucidated mechanism differences under three adsorption configurations. $^1$O$_2$ (2.97×10$^{-9}$ M), SO$_4^{\bullet-}$ (2.09×10$^{-11}$ M) and $^\bullet$OH (7.36×10$^{-12}$ M) dominated the E-REM-PMS system, consistent with sequence of reactive species by DFT results. Continuous treatment of pharmaceutical wastewater confirmed 100% CBZ removal and 60%-70% TOC mineralization at ultrahigh water flux (642.86 L/m$^2$·h) with minimal energy consumption (0.01 kWh/m$^3$·order). This work proposed a high-performance and anti-fouling REM, offering an efficient and economical solution for wastewater treatment.

## 1. Introduction

Peroxymonosulfate (PMS)-based advanced oxidation processes (AOPs) are drawing immense attention to eliminate refractory contaminants through triggering different pathways [1,2], generating powerful reactive oxygen species (ROS) with redox potentials of 1.8 ∼ 3.1 V vs. NHE [3], including sulfate radical (SO$_4^{\bullet-}$), hydroxyl radical ($^\bullet$OH), superoxide radical (O$_2^{\bullet-}$) and non-radical singlet oxygen ($^1$O$_2$) [4,5]. Transition metals have been widely used in PMS activation to overcome the high cleavage energy, of which cobalt is regarded as the most promising [6]. However, the following challenges still remain in the heterogeneous cobalt catalyst: (i) low activation efficiency of PMS owing to the insufficient utilization of active sites; (ii) application limitations of catalyst reusability and poor performance in complex wastewater treatment [7].

Various strategies have been executed to enhance PMS activation, among which designing a highly efficient cobalt-based catalyst is the most direct and significant. Perovskite oxides (ABO$_3$) have been extensively utilized for PMS activation and showed significant potential in practical wastewater treatment [8]. Perovskites possessed excellent structure flexibility since the A and B sites can accommodate a wide range of metals, where A is a rare-earth or alkaline earth element and B is a transition metal. The A-site predominantly serves to stabilize the crystal structure of perovskite, whereas the B-site functions as the primary active site for catalysis [9]. The variation of A or B sites will affect the physicochemical properties of perovskites. For A-site, LaCoO$_3$ showed faster reaction rate for phenol degradation than that of CeCoO$_3$ and BaCoO$_3$ [10]. For B-site, LaCoO$_3$ was the most active catalysts among LaMO$_3$ (M=Co, Fe, Cu and Mn) perovskites with exceptional reusability and low metal leaching [11]. Hence, LaCoO$_3$ would be an outstanding catalyst to efficiently activate PMS for contaminants

---

elimination.

Considering the complex matrix of actual wastewater, PMS approach alone may not achieve satisfactory decontamination [12]. To further promote the activation kinetics of PMS and the mass transport performance, a novel reactive electrochemical membrane (REM) system has been proposed as a breakthrough in electrochemical water treatment because its mass transfer rate ($k_m$) is $1-2$ orders of magnitude larger than the $k_m$ ($10^{-5}$ m/s) in a flow-by system [13]. The REM system can also improve the oxidation kinetics by $\sim 10$ times, reduce the electric energy cost by $\sim 90$ % [14], and alleviate the membrane pollution due to the electrostatic repulsion between charged pollutants and the membrane electrode [15].

Magnéli phase titanium oxide $Ti_4O_7$, as a typical REM, exhibits outstanding potential for electrochemical oxidation due to its excellent electric conductivity (1500 S/cm), high redox potential (2.5 V vs. Ag/AgCl), and corrosion resistance [16,17], making it effective in degrading contaminants [18]. $Ti_4O_7$ as a potential anode REM can produce ROS by direct electron transfer, but the generated ROS are insufficient to rapidly and efficiently remove contaminants due to poor electron mobility and the lack of reactive sites [19]. Notwithstanding the commendable electrochemical stability and cost-effectiveness of $Ti_4O_7$, its comparatively constrained electro-oxidation capability resulted in prolonged wastewater purification periods. Coincidentally, PMS is recognized as an effective approach for enhancing water treatment performance. Based on the above analysis, it would be reasonable to propose a perovskite-functionalized REM to enhance the activation efficiency of PMS, simultaneously promoting the removal of micropollutants with high efficiency and low energy consumption while maintaining the stability of REM and overcoming the application limitations of catalyst recovery and water matrix interference in actual wastewater treatment.

Herein, in this work, $Ti_4O_7$ was selected as the membrane substrate, and a small quantity of $LaCoO_3$ was introduced as an exceptional catalyst to efficiently activate PMS in a flow-through mode. An enhanced carbamazepine (CBZ) degradation was envisaged due to the synergistic effects of $LaCoO_3/Ti_4O_7$ REM, PMS and the electric field. The superiority of electro-enhanced activation process of PMS by $LaCoO_3/Ti_4O_7$ REM (E-REM-PMS) system and the reaction mechanism were proposed based on experimental results, electron paramagnetic resonance (EPR), density functional theory (DFT) calculations and *in-situ* Fourier Transform Infrared Spectroscopy (FTIR). The degradation pathway and toxicity assessment were also analyzed. The practical application prospect was evaluated by taking water quality tolerance, energy consumption and durability into account. This work provides a strategy to create an economical, effective and environmentally friendly continuous-flow system for water decontamination.

## 2. Experimental section

### 2.1. Chemicals and materials

All the chemicals and reagents used in the experiments were analytical grade, and the detailed information was provided in Text S1. Deionized water (DI water) was employed throughout the research.

### 2.2. Synthesis of $Ti_4O_7$ and $LaCoO_3/Ti_4O_7$ REMs

The $Ti_4O_7$ REM was synthesized by firstly mixing 10 g $Ti_4O_7$ powder with 2 mL paraffin oil as a binder. The powder and binder were thoroughly mixed for 20 min using mortar and pestle. The resulting mixture was then loaded into a stainless-steel die with a diameter of 3.8 cm. To compact the mixture, a uniaxial pressure of approximately 8 MPa was achieved using a hydraulic press (769YP-15A, Xinnuo, Shanghai, China). Subsequently, the pellet, with a thickness of 1.9 mm, underwent calcination in a tube furnace at 800 °C for 6 h under 1.0 atm Ar. This calcination step aimed to remove the binder and promote particle sintering, thereby achieving successful synthesis of $Ti_4O_7$ REM.

The $LaCoO_3$ perovskite was produced via a typical sol-gel process. Stoichiometric amounts of $La(NO_3)_3 \cdot 6 H_2O$ and $Co(NO_3)_2 \cdot 6 H_2O$ were dissolved in 30 mL deionized water under magnetic stirring. An equal amount of citric acid monohydrate (metal/citric acid molar ratio = 1/1) was added into the solution, then ultrasonically dispersing for 30 min. The resultant mixture was continuously stirred and condensed at 70 °C in a water bath for 4 h to evaporate water until the wet gel formed. Then dried it in an oven at 60 °C overnight. Subsequently, the powders were calcined at 800 °C for 2 h with a heating rate of 5 °C/min in a muffle furnace. Different qualities of the as-received $LaCoO_3$ were evenly mixed with 10 g $Ti_4O_7$ powder for 10 min. 2 mL paraffin oil was added and mixed with the powders for 20 min. Then the mixture was also placed in a die, pressed and calcined using the same method as the $Ti_4O_7$ REM (Fig. S1). *In-situ* FTIR spectroscopy, scanning electron microscopy (SEM), transmission electron microscopy (TEM), high-resolution TEM (HRTEM), X-ray diffractometer (XRD) and the Brunauer-Emmett-Teller (BET) method were performed to explore the characteristics of REMs. Details of the characterization methods for the REMs were illustrated in Text S2.

### 2.3. Electro-PMS activation for CBZ removal

The treatment of 0.1–20 mg/L CBZ was carried out at room temperature via activating PMS in a flow-through reactor as schematically shown in Fig. 1. $LaCoO_3/Ti_4O_7$ REM ($\Phi$30 mm, thickness: 1.9 mm) and carbon felt (CF) were installed in the reactor as anode and cathode respectively with an electrode spacing of 8 mm. Unless specifically stated, a neutral solution of CBZ (20 mg/L) containing PMS (2 mM) was passed through the filtration system at flowrate of 7.5 mL/min under a constant current of 5 mA. In the mixture of CBZ and PMS, 2 mM PMS alone exhibited negligible degradation of 20 mg/L CBZ within 120 min (Fig. S2). The PMS acted two roles, i.e., as a catalyst for ROS activation and as an electrolyte. The adjustment of pH was performed by NaOH (0.1 mol/L) and $H_2SO_4$ (0.1 mol/L). At given time period, 0.5 mL of reaction solution was withdrawn and quenched with 1 mL methanol (MeOH) and 0.5 mL 50 mM L-histidine (L-His). Afterwards, the sample was filtered through a 0.22 μm membrane for further measurement. The concentration of CBZ was analyzed using high-performance liquid chromatography (HPLC, Ultimate 3000, ThermoFisher, America) with C18 column (3 μm, $\phi 3.0 \times 100$ mm) equipped with a DAD detector. The specific analytical parameters were provided in Table S1. Residual PMS was quantified by an iodometric method, and the resulting absorbance was measured at 352 nm using a UV–Vis spectrophotometer (UV835, Shanghai Lab-Spectrum Instrument Co., Ltd.). The calculation of hydraulic residence time, rate constant, synergistic factor, electric energy consumption and water flux were displayed in Text S3.

The effects of parameters (e.g., solution pH, current density, PMS dose and flow rate), co-existing ions ($SO_4^{2-}$, $Cl^-$, $NO_3^-$, $CO_3^{2-}$ and $PO_4^{3-}$) and natural organic matters (humic acid (HA) and fulvic acid (FA)) were investigated. The system was also applied to treat actual pharmaceutical wastewater, and the durability of $LaCoO_3/Ti_4O_7$ REM was tested through consecutive CBZ removal for 10 hours. The used REMs were washed with DI water and dried naturally before initiating a new cycle. The versatility of the process was evaluated by degrading other refractory pharmaceuticals (20 mg/L), including sulfamethazine (SMT), sulfamethoxazole (SMX), atrazine (ATZ) and tetracycline (TC). All experiments were conducted in triplicate. The relevant analytical methods and electrochemical measurements were given in Text S3. The quantitative analysis of ROS was presented in Text S4. The operational methods of *in-situ* FTIR spectroscopy were described in Text S5. The details of DFT calculations were provided in Text S6.
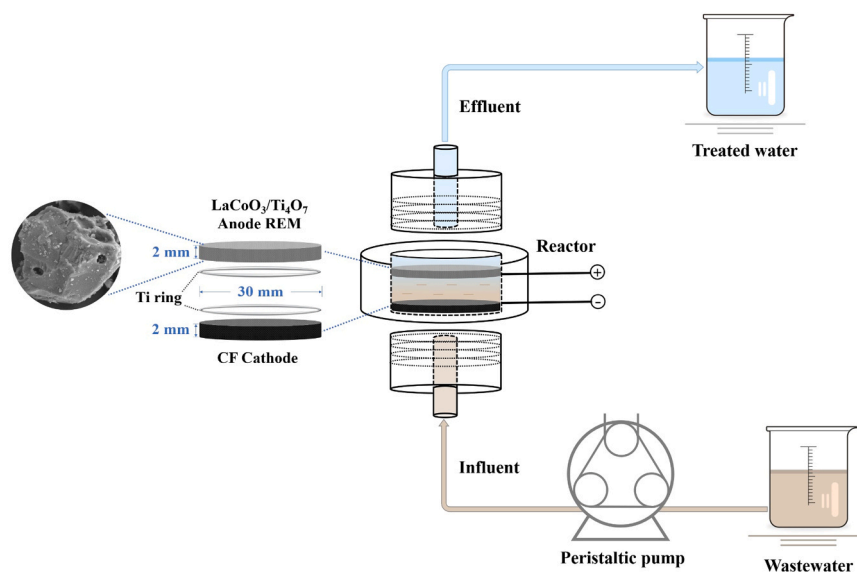
**Fig. 1.** The schematic diagram of the reaction process.

## 3. Results and discussion

### 3.1. Characterization and properties of the LaCoO₃/Ti₄O₇ REM

To verify the successful synthesis of LaCoO$_3$/Ti$_4$O$_7$, the structure, composition and morphology of prepared REMs were investigated by SEM, TEM, XRD and N$_2$ adsorption-desorption isotherm. It was observed that Ti$_4$O$_7$ showed micron-sized particles with a smooth surface (Fig. 2a and S3a). In Fig. 2b-c and S3b-d, the rough surface of LaCoO$_3$/Ti$_4$O$_7$ might be ascribed to the nanoparticles of LaCoO$_3$. Massive structured Ti$_4$O$_7$ serves as the base of the composite, while LaCoO$_3$ distributes on its surface as the active sites for PMS activation. The surface of the LaCoO$_3$/Ti$_4$O$_7$ REM displayed distinct microporous morphology. In high-resolution SEM images, pore-like structures resembling cracks can be observed, possibly arising from the volatilization of paraffin oil binder during electrode calcination processes (Fig. S3b-d). The lattice spacings of 0.338 nm and 0.272 nm in the high-resolution transmission electron microscopy (HRTEM, Fig. 2d) images are associated with Ti$_4$O$_7$ (1 −2 0) and LaCoO$_3$ (1 1 0), respectively. The energy dispersive spectroscopy (EDS) of LaCoO$_3$/Ti$_4$O$_7$ in Fig. 2e depicted that the elements of Ti, La, Co and O are evenly distributed on the surface. As calculated, the loading amounts of La and Co in a LaCoO$_3$/Ti$_4$O$_7$ REM are approximately 8.5 mg and 3.6 mg, which correspond to 0.085 wt% and 0.036 wt%, respectively. The loading amount of catalyst is significantly lower compared to the similar electro-activated PMS processes such as Fe-SA/Mo$_2$TiC$_2$T$_x$ filter (1.8 wt% Fe) [7] and Fe$_3$O$_4$-MnO$_2$/CNT filter (2.8 wt% Fe, 3.2 wt% Mn) [20].

As shown in Fig. 2f, the sharp XRD patterns illustrated well crystalline natures of 0.15 wt% LaCoO$_3$/Ti$_4$O$_7$, LaCoO$_3$ and Ti$_4$O$_7$. The Ti$_4$O$_7$ showed well characteristic diffraction peaks of Ti$_4$O$_7$ phase (JCPDS No. 72–1722). The LaCoO$_3$ powders were also successfully synthesized, in accordance with the rhombohedral structure (lattice constants a = 5.4410 Å, b = 5.4410 Å, and c = 13.0880 Å) in the reference code (JCPDS No. 25–1060). When 0.15 wt% LaCoO$_3$ was mixed with Ti$_4$O$_7$, Ti$_4$O$_7$ still maintained the high-purity Magneli phases, indicating the introduction of 0.15 wt% LaCoO$_3$ did not oxidize or reduce Ti$_4$O$_7$. The diffraction peak corresponding to LaCoO$_3$ was a little weak in the obtained composite, mainly attributing to the minimal content of LaCoO$_3$. But if the XRD pattern of 0.15 wt% LaCoO$_3$/Ti$_4$O$_7$ was magnified (Fig. S4), the peaks of LaCoO$_3$ obviously existed at 23.2°, 32.9°, 33.3°, 47.5° and 59.0°.

To assess the adsorption and degradation properties of LaCoO$_3$/Ti$_4$O$_7$, two significant indexes of specific surface area and pore structure were explored. As revealed in Fig. 2g, the N$_2$ adsorption-desorption isotherm of 0.15 wt% LaCoO$_3$/Ti$_4$O$_7$ conformed to the typical type II curve with H4 hysteresis loop according to the IUPAC classification. The BET surface area of LaCoO$_3$/Ti$_4$O$_7$ was 1.72 m$^2$/g, higher than the 0.54 m$^2$/g of pure Ti$_4$O$_7$. Fig. 2g inset showed that Ti$_4$O$_7$ displayed a pore size distribution spanning from 2.3 to 57.5 nm, demonstrating solely mesoporous characteristics. In regard to LaCoO$_3$/Ti$_4$O$_7$, the pore size ranged from 1.7 nm to 28.3 nm, with micropores accounting for 16% and mesopores for 84%. The introduction of LaCoO$_3$ resulted in the emergence of micropores, accompanied by a significant increase in pore structures below 10 nm. The multistage porous structure of LaCoO$_3$/Ti$_4$O$_7$ REM is conducive to transfer between pollutants and oxidants as wastewater passed through REM.

Electrochemical measurements were conducted to assess the reactivity of the pristine Ti$_4$O$_7$ and LaCoO$_3$/Ti$_4$O$_7$ REM. As the linear sweep voltammetry (LSV) spectra displayed in Fig. S5a, LaCoO$_3$/Ti$_4$O$_7$ exhibited a slightly higher oxygen evolution potential (OEP) of 2.05 V vs Ag/AgCl than 1.95 V of pristine Ti$_4$O$_7$. Open circuit electrochemical impedance spectroscopy (EIS) measurements were conducted to characterize the electron transport and electron transfer of the pristine Ti$_4$O$_7$ and LaCoO$_3$/Ti$_4$O$_7$. From Fig. 2h, LaCoO$_3$/Ti$_4$O$_7$ revealed a charge transfer resistance ($R_{ct}$) of 95.43 Ω, which was lower than the 98.84 Ω of Ti$_4$O$_7$. Despite the doping amount of LaCoO$_3$ being only 0.15 wt%, an observable reduction in resistance was observed. The lower $R_{ct}$ is more conducive to improving the catalytic activity and electron transfer kinetics. Cyclic voltammetry (CV) presented in Fig. S5b showed an improved anodic peak current ($I_{pa}$) on the LaCoO$_3$/Ti$_4$O$_7$ electrode, which increased by about 1.5 times, indicating an enhanced electrochemical reactivity compared with the pristine Ti$_4$O$_7$ electrode. The CV curves also elucidated that the LaCoO$_3$/Ti$_4$O$_7$ electrode had a larger electroactive area than Ti$_4$O$_7$ electrode, certifying that LaCoO$_3$ provided additional reactive sites on the surface of Ti$_4$O$_7$.

### 3.2. Electro-PMS activation performance of LaCoO₃/Ti₄O₇ REM

CBZ was selected as the model micropollutant to evaluate the catalytic performance of the LaCoO$_3$/Ti$_4$O$_7$ REM toward electro-PMS activation. As depicted in Fig. 3a, marginal CBZ removal (<2%) was observed in the presence of LaCoO$_3$/Ti$_4$O$_7$ REM or PMS alone, suggesting that contributions from the adsorption and PMS oxidation were negligible. About 11% CBZ removal occurring in electro-activation of
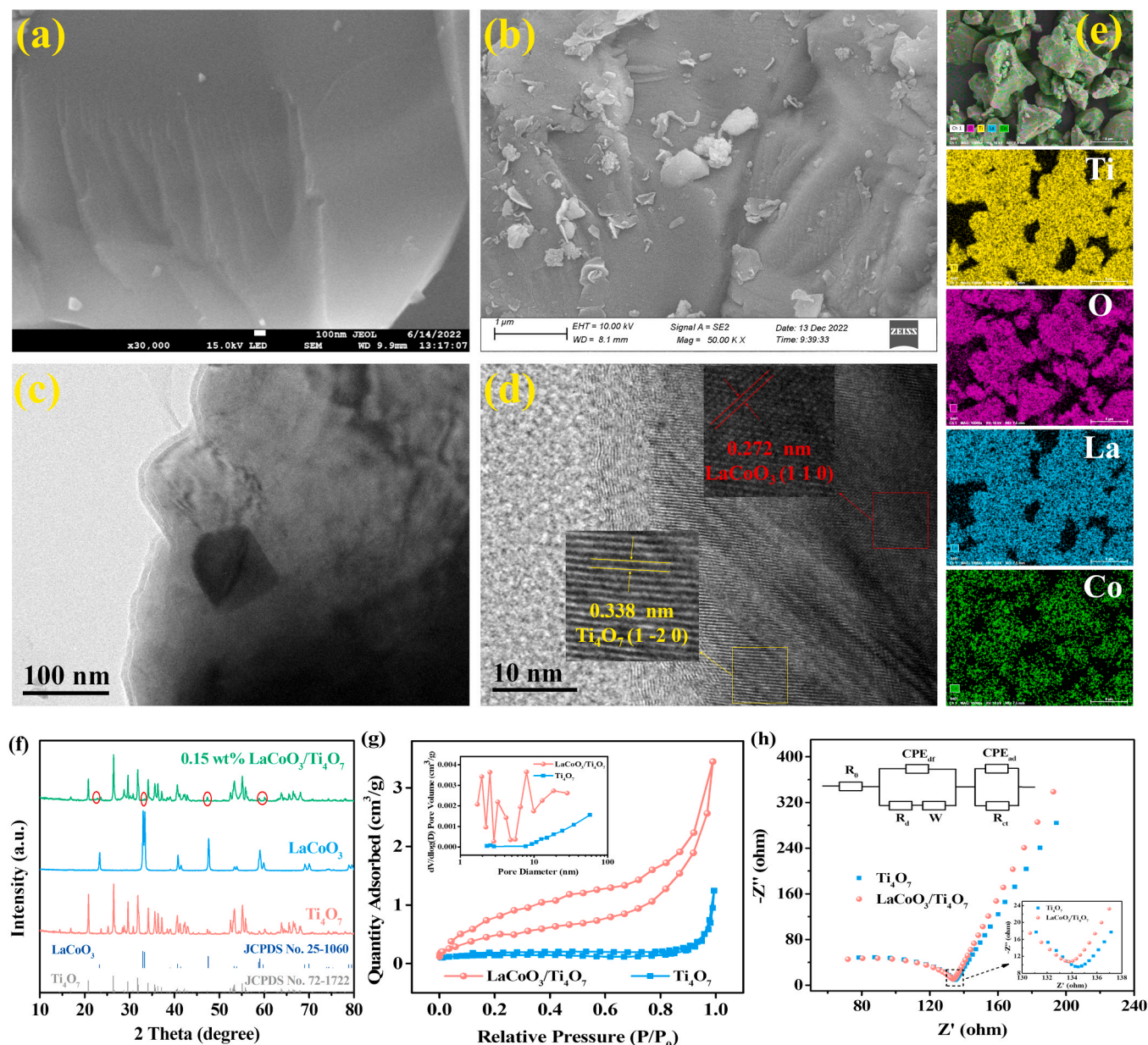
**Fig. 2.** SEM of pure $Ti_4O_7$ (a), SEM (b) TEM (c), HRTEM (d) and EDS mappings (e) of 0.15 wt% $LaCoO_3/Ti_4O_7$, XRD patterns of 0.15 wt% $LaCoO_3/Ti_4O_7$, $LaCoO_3$ and $Ti_4O_7$ (f), $N_2$ adsorption-desorption isotherm for $LaCoO_3/Ti_4O_7$ with pore size distribution (inset) (g) and Open circuit EIS measurements (h).

PMS by $Ti_4O_7$ REM (E-$Ti_4O_7$-PMS) system was still dissatisfactory, but the introduction of $LaCoO_3$ significantly improved the catalytic activity. In Fig. S6, the CBZ removal increased with the dosage of $LaCoO_3$ increasing from 0 to 0.15%. As the dosage of $LaCoO_3$ increased to 0.15%, 100% CBZ degradation was obtained by a single pass through the E-$LaCoO_3/Ti_4O_7$-PMS system at a current density 0.5 mA/cm². When the content of $LaCoO_3$ exceeded 0.15%, the complete decomposition of CBZ could also be maintained within 120 min. Combined with economic and environmental benefits, 0.15% $LaCoO_3/Ti_4O_7$ REM was selected as the optimized anode and utilized in the subsequent E-REM-PMS system if not specified.

The E-REM-PMS system possessing excellent CBZ elimination (~100 %) and short hydraulic retention time ($\tau$ ~ 10.6 s) confirmed the enhanced removal performance of the integrated system. The removal efficiency of CBZ decreased to ~30 % and 3 % in the absence of electric field and PMS, which were both dissatisfied. Data from the CBZ removal experiments were fitted to pseudo-first-order kinetics for quantitative comparison of the different systems [21]. The apparent rate constant ($k$)

for CBZ removal in the E-REM-PMS system (39.69 min⁻¹) was 233 and 23 times of electro-REM (E-REM) system (0.17 min⁻¹) without PMS addition and REM activating PMS (REM-PMS) system (1.7 min⁻¹) without electricity input, respectively. The TOC removal reached 45 % by a single pass through the E-REM-PMS system during CBZ degradation, which was more than three times that in the other systems (Fig. 3b). Applying a very low current density of 0.5 mA/cm² enhanced 73 % CBZ removal and 32 % TOC mineralization. The synergistic factor (S) was calculated from Eq. (S5) to quantify the interaction degree of electric field and PMS [22]. The high S (21.22) was attributed to the electro-enhanced activation of PMS by $LaCoO_3/Ti_4O_7$ REM, which significantly accelerated the degradation and mineralization kinetics of CBZ. These results illustrated that the $LaCoO_3/Ti_4O_7$ REM can serve as a superior catalyst for electro-PMS activation, highlighting the evident synergistic effect between the PMS and electric field.

The significant difference between E-REM-PMS and REM-PMS system suggested that the electric field played an important role in the degradation of CBZ. As the applied current density increasing from 0 to
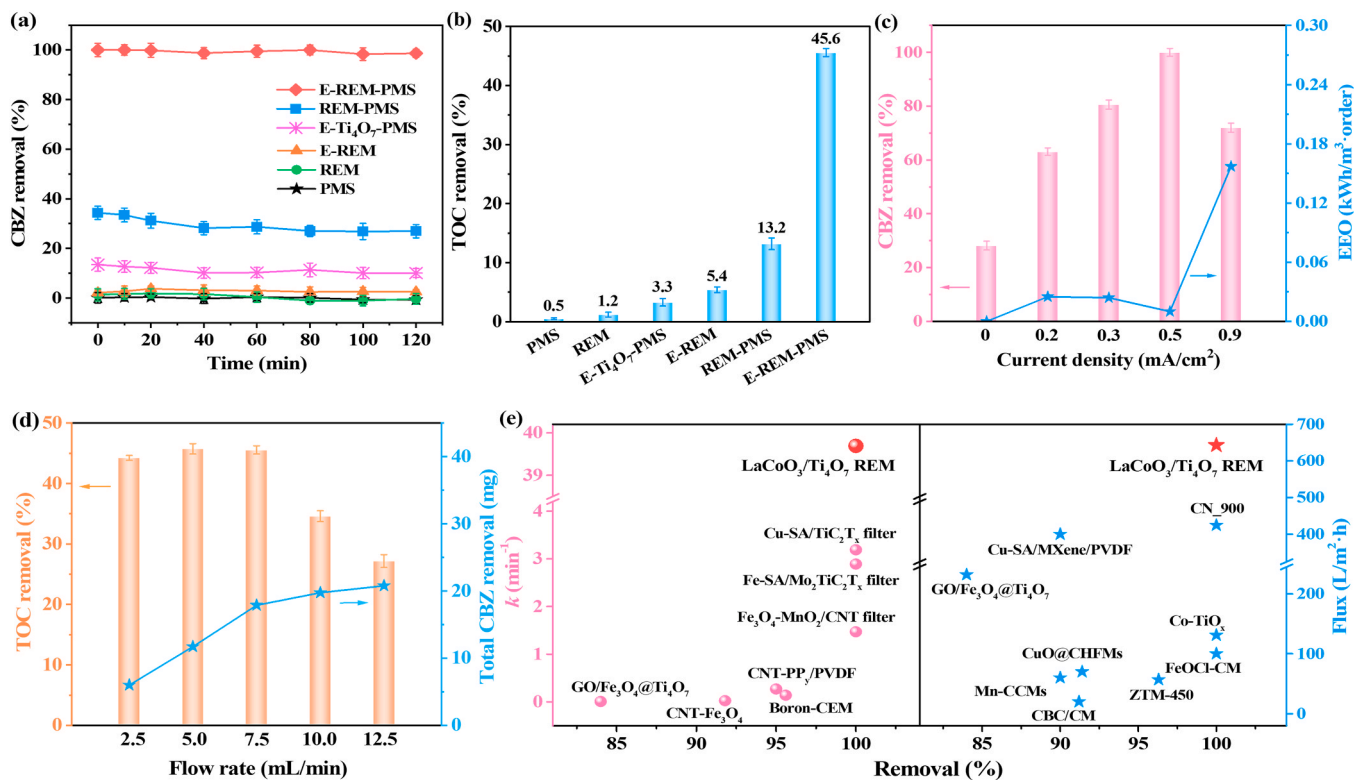
**Fig. 3.** CBZ removal (a) and TOC mineralization (b) in different reaction systems. Reaction conditions: [CBZ] = 20 mg/L, [PMS] = 2 mM, flow rate = 7.5 mL/min, influent solution pH = 7, current density = 0.5 mA/cm². CBZ removal influenced by applied current density (c), TOC mineralization and total removal quality of CBZ within 120 min under different flow rate (d) and the rate constant and flux of $LaCoO_3/Ti_4O_7$ REM compared with the literature (e).

0.5 mA/cm², the CBZ removal was improved from 28% to 100% (Fig. 3c). The trend of PMS consumption was consistent with the CBZ removal, further suggesting that the electric field promoted the decomposition of PMS (Fig. S8a). The minimum energy consumption occurred at 0.5 mA/cm², indicating that it was the optimal current density for achieving the highest removal efficiency. Compared to the batch mode, the efficient convection-enhanced mass transport improved the performance of the flow-through system [7]. The flow rate determined the contact time between contaminants and REM, and excessive flow rate led to inadequate reaction of ROS. Notably, when the flow rate varying from 2.5 to 7.5 mL/min, the degradation efficiency of CBZ in single-pass mode maintained ~100% and the TOC mineralization was around 45% (Fig. 3d and S7a). With the flow rate exceeding 7.5 mL/min, decreases appeared both in the oxidation efficiencies of CBZ and TOC. Besides, the PMS decomposition obviously weakened at high flow rates of 10.0 and 12.5 mL/min, further illustrating the insufficient contact when PMS flowing through REM (Fig. S8b). The total removal quantity of CBZ within 120 min greatly enhanced from 5.99 mg to 17.87 mg as the flow rate increasing from 2.5 to 7.5 mL/min. While the flow rate raised to 12.5 mL/min, the CBZ removal slowly reached 20.7 mg (Fig. 3d). Despite a slight increase in the total removal quality of CBZ at flow rates exceeding 7.5 mL/min, the excessively high flow rate was unable to achieve complete elimination of CBZ. Consequently, a flow rate of 7.5 mL/min was identified as the preferred option, striking commendable performances in both removal efficiency and total removal quality of CBZ. PMS also played a crucial role in the E-REM-PMS system. As depicted in Fig. S7b, the CBZ removal was markedly enhanced from ~3% to 100% with the PMS dosage increasing from 0 to 2 mM. However, a further increase of PMS dosage to 3 mM brought a reduction in CBZ degradation instead, which might be attributed to the self-quenching effect between the generated radicals and excess PMS ($HSO_5^- + SO_4^{\bullet-} \rightarrow SO_4^{2-} + SO_5^{\bullet-} + H^+$, $HSO_5^- + {}^{\bullet}OH \rightarrow SO_5^{\bullet-} + H_2O$) [23]. From the PMS consumption in Fig. S8c, it was noticed that slight PMS was not sufficient to produce enough ROS to completely remove CBZ, and excessive PMS led to competition between CBZ and surplus PMS. Hence, current density of 0.5 mA/cm², flow rate of 7.5 mL/min and PMS of 2 mM were identified as the optimal parameters for subsequent experiments.

Energy consumption is another important parameter to judge the feasibility of electrochemical technology in practical wastewater treatments. The E-REM-PMS system exhibited an impressively low energy consumption (electrical energy per order, EEO) of 0.01 ± 0.001 kWh/m³·order (Eq. (S6)), which was merely 2.7% of advanced Cu-SA/$Ti_3C_2T_x$ filter (0.37 kWh/m³·order) and 3.6% of $Fe_3O_4$-$MnO_2$/CNT filter (0.28 kWh/m³·order) in the same single-pass mode (Table 1) [20,21]. The remarkable energy efficiency of the E-REM-PMS system positioned it as a superior alternative to conventional filtration technologies. Additionally, the E-REM-PMS system achieved a remarkable rate constant of 39.69 min⁻¹, surpassing other processes in Fig. 3e by over tenfold. Less reagent use (2 mM) and lower current application (0.5 mA/cm²) can greatly improve the removal efficiency compared to the E-REM system and REM-PMS system. The water flux of $LaCoO_3/Ti_4O_7$ REM (642.86 L/m²·h) was the highest in Fig. 3e and outperformed state-of-the-art membrane processes, such as the electrocatalytic oxidation using carbon-nanofiber-based membrane CN_900 (424.5 L/m²·h) and PMS activation by the Cu-SA/MXene-900/PVDF membrane (357–400 L/m²·h) (Table S4) [24,25]. The enhanced capability enabled the E-REM-PMS system to rapidly and efficiently process larger volumes of sewage, showing great potential for the practical applications.

### 3.3. Mechanism study

#### 3.3.1. Qualitative and quantitative identification of ROS

Quenching experiments were conducted to identify the ROS during the electro-PMS-activated removal of CBZ using $LaCoO_3/Ti_4O_7$ REM.

**Table 1**
Performance comparison of electro-PMS catalytic membrane with the literature.

| Anode | Cathode | pollutant | Conditions | Regent | Removal | $k$ (min$^{-1}$) | Energy consumption | Ref. |
|---|---|---|---|---|---|---|---|---|
| Titanium mesh | MnFe$_2$O$_4$-rGO membrane | Oxytetracycline (10 mg/L) | pH 7, Voltage 3 V | PMS 0.98 mM, K$_2$SO$_4$ 0.57 mM | 88.3 % (100 min) | | | [26] |
| Ti/RuO$_2$-IrO$_2$ plate (3.14 cm$^2$) | GO/Fe$_3$O$_4$@Ti$_4$O$_7$ membrane (3.14 cm$^2$) | 1,4-dioxane (88 mg/L) | pH initial, current density 20 mA/cm$^2$ | PMS 25 mM, Na$_2$SO$_4$ 20 mM | 84 % (180 min) | 7.21×10$^{-3}$ | - | [27] |
| Perforated titanium plate | CNT-Fe$_3$O$_4$ filter | Roxarsone (1.5 mg/L) | Voltage −1 V | PMS 1.5 mM | 91.8 % (120 min) | 0.025 | - | [28] |
| Graphite | Graphite | Ni-EDTA (0.1 mM) | pH 2.3, boron 1 g/L, Boron/PMS-electrolysis membrane, current density 6.887 mA/cm$^2$ | PMS 30 mM, Na$_2$SO$_4$ 50 mM | 95.6 % (40 min) | 0.1399 | - | [29] |
| Ti plate | CNT cross-linked polypyrrole membrane (CNT-PPy/PVDF) | Carbamazepine (2 mg/L) | pH 3.2, current density 2.3 mA/cm$^2$ | PDS 50 mM | >95 % | ~0.27 | 0.1193 kWh/m$^3$ | [30] |
| Porous titanium mesh | Pd-ceramic membrane | Methylene Blue (3.2 mg/L) | pH 5.7, Voltage 1.6 V, flow rate 0.8 mL/min | PMS 0.1 mM, Na$_2$SO$_4$ 10 mM | 94.5 % (23 s) | - | 1.78 kWh/kg | [31] |
| Perforated titanium sheet | Fe$_3$O$_4$-MnO$_2$/CNT filter | Sulfamethoxazole (10 mg/L) | pH 6.2 ± 0.1, Voltage 1.5 V, 1.1 mA, flow rate 1.5 mL/min | PMS 1.5 mM | 100 % (2 s) | 1.47 | 0.28 kWh/m$^3$·order | [20] |
| Perforated titanium sheet | Fe-SA/ Mo$_2$TiC$_2$T$_x$ filter | Sulfamethoxazole (15 mg/L) | Voltage 2 V, flow rate 1.5 mL/min | PMS 1 mM, K$_2$SO$_4$ 0.57 mM | 100 % (2 s) | 2.89 | 0.003 kWh/kg SMX | [7] |
| Perforated titanium sheet | Cu-SA/ Ti$_3$C$_2$T$_x$ filter | Sulfamethoxazole (10 mg/L) | pH 6.2 ± 0.2, Voltage 1 V, flow rate 1.5 mL/min | PMS 1.5 mM | 100 % (150 ms) | 3.19 | 0.37 kWh/m$^3$·order | [21] |
| LaCoO$_3$/Ti$_4$O$_7$ REM (7 cm$^2$) | CF (7 cm$^2$) | Carbamazepine (20 mg/L) | pH 7, current density 0.5 mA/cm$^2$, flow rate 7.5 mL/min | PMS 2 mM | 100 % (10.6 s) | 39.69 | 0.01 ± 0.001 kWh/m$^3$·order | This work |
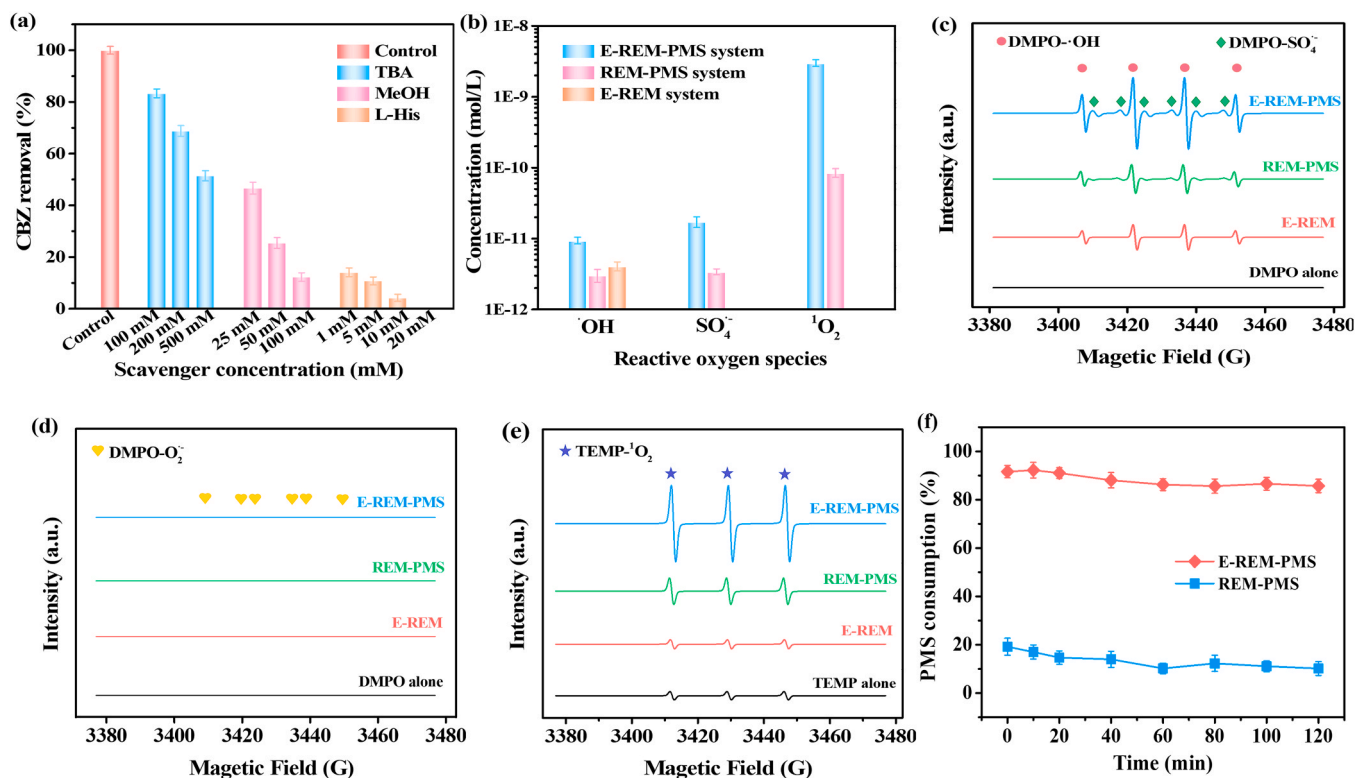


**Fig. 4.** The effect of different concentration TBA, MeOH and L-His (a) as scavengers on CBZ degradation in the E-REM-PMS system. Reaction conditions: [CBZ] = 20 mg/L, [PMS] = 2 mM, flow rate = 7.5 mL/min, influent solution pH = 7, current density = 0.5 mA/cm$^2$. The steady-state concentrations of $\cdot$OH, SO$_4^{\cdot-}$ and $^1$O$_2$ in the E-REM-PMS system using NB, BA and FFA as probes (b). EPR spectra of DMPO-$\cdot$OH or DMPO-SO$_4^{\cdot-}$ (c), DMPO-O$_2^{\cdot-}$ (d), TEMP-$^1$O$_2$ (e) at 60 min in the different systems, and PMS consumption in the E-REM-PMS and REM-PMS systems (f).

Methanol (MeOH) can efficiently scavenge both $^\bullet$OH ($k_{\bullet OH} = 9.7 \times 10^8$ $M^{-1}$ $s^{-1}$) and $SO_4^{\bullet-}$ ($k_{SO_4^{\bullet-}} = 3.2 \times 10^7$ $M^{-1}$ $s^{-1}$), while tert-butanol (TBA) is more selective toward $^\bullet$OH ($k_{\bullet OH} = 3.8 \times 10^8$ $M^{-1}$ $s^{-1}$) compared with $SO_4^{\bullet-}$ ($k_{SO_4^{\bullet-}} = 4 \times 10^5$ $M^{-1}$ $s^{-1}$) [7]. Fig. 4a showed that the CBZ degradation was weakened with the TBA concentration increasing from 100 to 500 mM, elucidating $^\bullet$OH contributed to the CBZ degradation in the E-REM-PMS system. MeOH exhibited a stronger inhibition than TBA with the increasing dosage, and the CBZ removal just maintained ~10 % in the presence of 100 mM MeOH. The apparent inhibition gap between MeOH and TBA implied that $SO_4^{\bullet-}$ was one of the major ROS in the system. Additionally, the introduction of L-Histidine (L-His) as a $^1O_2$ quencher ($k_{^1O_2} = 1.5 \times 10^8$ $M^{-1}$ $s^{-1}$) had a significant suppression on CBZ removal. The degradation of CBZ was almost 100 % inhibited by 20 mM L-His, and even 1 mM L-His can still achieve ~85 % inhibition effect. Consequently, $^1O_2$ should be the dominant ROS responsible for CBZ degradation in this system. Furthermore, the negligible effect from superoxide dismutase (SOD), a quencher of $O_2^{\bullet-}$, indicated no significant contribution to CBZ degradation by $O_2^{\bullet-}$ (Fig. S9). Hence, $^1O_2$, $SO_4^{\bullet-}$ and $^\bullet$OH are the major ROS in the E-REM-PMS system.

Nitrobenzene (NB), benzoic acid (BA) and furfuryl alcohol (FFA) were further chosen as probes to quantify the above major ROS. The steady-state concentrations of $^\bullet$OH ([$^\bullet$OH]$_{ss}$), $SO_4^{\bullet-}$ ([$SO_4^{\bullet-}$]$_{ss}$) and $^1O_2$ ([$^1O_2$]$_{ss}$) in the E-REM-PMS system can be obtained as Eqs. (S8)-(S10) [32,33]. The rate constants for the degradation of NB, BA and FFA were 1.72, 2.43, and 40.55 $min^{-1}$, respectively (Fig. S10). As calculated, approximately $7.36 \times 10^{-12}$ M of [$^\bullet$OH]$_{ss}$, $2.09 \times 10^{-11}$ M of [$SO_4^{\bullet-}$]$_{ss}$ and $2.97 \times 10^{-9}$ M of [$^1O_2$]$_{ss}$ were detected in this system (Fig. 4b). The steady-state concentrations in the E-REM-PMS system follow the sequence $^1O_2 > SO_4^{\bullet-} > ^\bullet$OH, consistent with the results of quenching experiments (Fig. 4a). Possible reaction mechanisms of $^1O_2$ have been reported: (i) ene reaction (reaction with alkene), (ii) endoperoxide formation (reaction with 1,3-dienes), (iii) sulfide oxidation, and (iv) electron transfer. Owing to the 1,3-diene moiety in the CBZ molecule, $^1O_2$ potentially reacted with 1,3-dienes to form endoperoxides (~$10^8$ $M^{-1}$ $s^{-1}$) [34,35].

Direct electron transfer has been reported to mediate organic degradation when contaminants and activated PMS coexist on the catalyst surface [32]. Chronoamperometric analysis was performed to assess the electron transfer process. As shown in Fig. S11, the injection of PMS induced a slight current response (~1.5 μA), which can be ascribed to the electron redistribution by the interaction between PMS and the LaCoO$_3$/Ti$_4$O$_7$ surface [36]. However, the subsequent addition of CBZ did not produce any obvious current response, manifesting that CBZ was not directly oxidized by the electron transfer process. These results confirmed that PMS can be directly activated by the electrons from LaCoO$_3$/Ti$_4$O$_7$, producing ROS for CBZ degradation [37]. Co(II)/peroxide systems have been found to enable the generation of high-valent cobalt (Co(IV)) in acid medium [38]. However, corresponding sulfone (PMSO$_2$) was not detected in the E-REM-PMS process by using 250 μM methyl phenyl sulfoxide (PMSO) as the chemical probes, further confirming the negligible role of Co(IV) (Fig. S12). In summary, $^1O_2$, $SO_4^{\bullet-}$ and $^\bullet$OH played the major roles in the E-REM-PMS system, and the ROS contributions to CBZ removal conformed to $^1O_2 > SO_4^{\bullet-} > ^\bullet$OH.

### 3.3.2. Synergistic effect between electric field and PMS

The water decontamination performance in Fig. 3a-3b has shown that electric field and PMS synergistically eliminated the CBZ and TOC in the E-REM-PMS system. To investigate the synergistic effect of electric field and PMS, EPR spin trapping experiments were performed to explore the ROS generated in the different systems using DMPO and TEMP to target $^\bullet$OH, $SO_4^{\bullet-}$, $O_2^{\bullet-}$ and $^1O_2$, respectively. As depicted in Fig. 4c-e, weak signals of DMPO-$^\bullet$OH, DMPO-$SO_4^{\bullet-}$ and TEMP-$^1O_2$ existed and dominated the reaction process in the REM-PMS system, and DMPO-$O_2^{\bullet-}$ disappeared in the absence of electric field. After applying a current of 5 mA, the $^\bullet$OH and $SO_4^{\bullet-}$ appeared, and the intensity of $^1O_2$

obviously strengthened. The signal of DMPO-$O_2^{\bullet-}$ was negligible in the E-REM-PMS system, which was coincident with the quenching experiment. To further discuss the role of electric field, we tested the consumption of PMS in the E-REM-PMS and REM-PMS systems. In Fig. 4f, less than 20% PMS was decomposed and used for the degradation of CBZ without electricity. As the applied current density increasing to 0.5 mA/cm$^2$, the PMS consumption rose to over 85% (Fig. S8a). More than 65% improvement of PMS utilization appeared after applying a current density of 0.5 mA/cm$^2$ (Fig. 4f). The introduction of electricity greatly accelerated the decomposition of PMS and facilitated the generation of ROS. This phenomenon might be attributed to that electric field gathered HSO$_5^-$ at the anode through electrostatic attraction, promoting the activation of PMS by LaCoO$_3$/Ti$_4$O$_7$ anode REM [39].

Except for electric field, the effect of PMS also cannot be ignored in the E-REM-PMS system. The DMPO-$O_2^{\bullet-}$ and TEMP-$^1O_2$ were absent in the E-REM system, and the intensity of DMPO-$^\bullet$OH was much lower than the E-REM-PMS system. Only 3% removal of CBZ in the E-REM system was achieved by the oxidation on LaCoO$_3$/Ti$_4$O$_7$ anode REM (Fig. 3a). PMS served as a prerequisite for the ROS, significantly improving the production of $^\bullet$OH, $SO_4^{\bullet-}$ and $^1O_2$. The steady-state concentrations of E-REM and REM-PMS system were calculated to evaluate the synergistic effect of electric field and PMS in depth. In Fig. 4b, only $4.09 \times 10^{-12}$ M of [$^\bullet$OH]$_{ss}$ without other ROS appeared in the E-REM system, in accordance with the EPR results. As for the REM-PMS system, the steady concentrations of $^\bullet$OH ($3.04 \times 10^{-12}$ M), $SO_4^{\bullet-}$ ($3.41 \times 10^{-12}$ M) and $^1O_2$ ($8.50 \times 10^{-11}$ M) were just 41.3%, 16.3% and 2.9% of those in the E-REM-PMS system, respectively. The results of synergistic factor, EPR analysis, ROS quantification and PMS utilization efficiency confirmed that both electric field and PMS play crucial roles in the E-REM-PMS system for water decontamination. Neither electric field nor PMS alone can effectively remove CBZ, but only the synergistic effect of both can completely degrade CBZ.

### 3.3.3. Proposed activation mechanisms

To examine the activation mechanism of PMS, *in-situ* FTIR spectroscopy was used to follow the evolution of the PMS on the effects of LaCoO$_3$/Ti$_4$O$_7$ and electric field. As shown in Fig. 5a, the peaks at 1254 and 1102 cm$^{-1}$ in the spectrum of PMS alone were indexed to the S−O bonds of HSO$_5^-$ and S-O bonds of SO$_4^{2-}$, respectively [7]. The bands observed around 2357 cm$^{-1}$ were assigned to CO$_2$ in air. When LaCoO$_3$/Ti$_4$O$_7$ was added, the slightly diminished intensity of HSO$_5^-$ indicated that LaCoO$_3$/Ti$_4$O$_7$ possessed the ability to activate PMS. To further illustrate the facilitating role of the electric field on the PMS activation by LaCoO$_3$/Ti$_4$O$_7$, real-time data acquisition by *in-situ* FTIR spectroscopy were conducted at a series of potentials (0–0.3 V). In Fig. 5b, a significant blue shift of PMS from 1254 to 1199 cm$^{-1}$ was observed with the increasing potential, which did not occur in the coexistence of LaCoO$_3$/Ti$_4$O$_7$ and PMS (Fig. 5a). It potentially suggested that electricity facilitated the PMS (HSO$_5^-$) to replace the −OH bonded to the catalyst surface and form a metastable $M^{n+}$−(HO)OSO$_3^-$ complex [40]. The broad upward peaks around 3300 cm$^{-1}$ originated from the correction of background peaks of $^\bullet$OH in H$_2$O molecule. Furthermore, the peak intensity of PMS rapidly decreased in the presence of electric field, which should be the consequence of the rapid decomposition of PMS. The reduction in PMS peak intensity provided additional evidence supporting the experimental results of PMS activation under the applied electric field. The bands at 885 and 1060 cm$^{-1}$ corresponding to the stretching vibration of S-O bond emerged upon applying an electricity and strengthened with the increasing potential, possibly due to the products of PMS decomposition. These results demonstrated that the electric field expedited the decomposition of PMS and the generation of $^1O_2$, $SO_4^{\bullet-}$ and $^\bullet$OH, leading to the ultrafast degradation of pollutants.

DFT simulation calculations were performed to analyze the adsorption configurations of PMS molecule on LaCoO$_3$/Ti$_4$O$_7$ REM and explore the probable formation mode of ROS. In the E-REM-PMS system, PMS
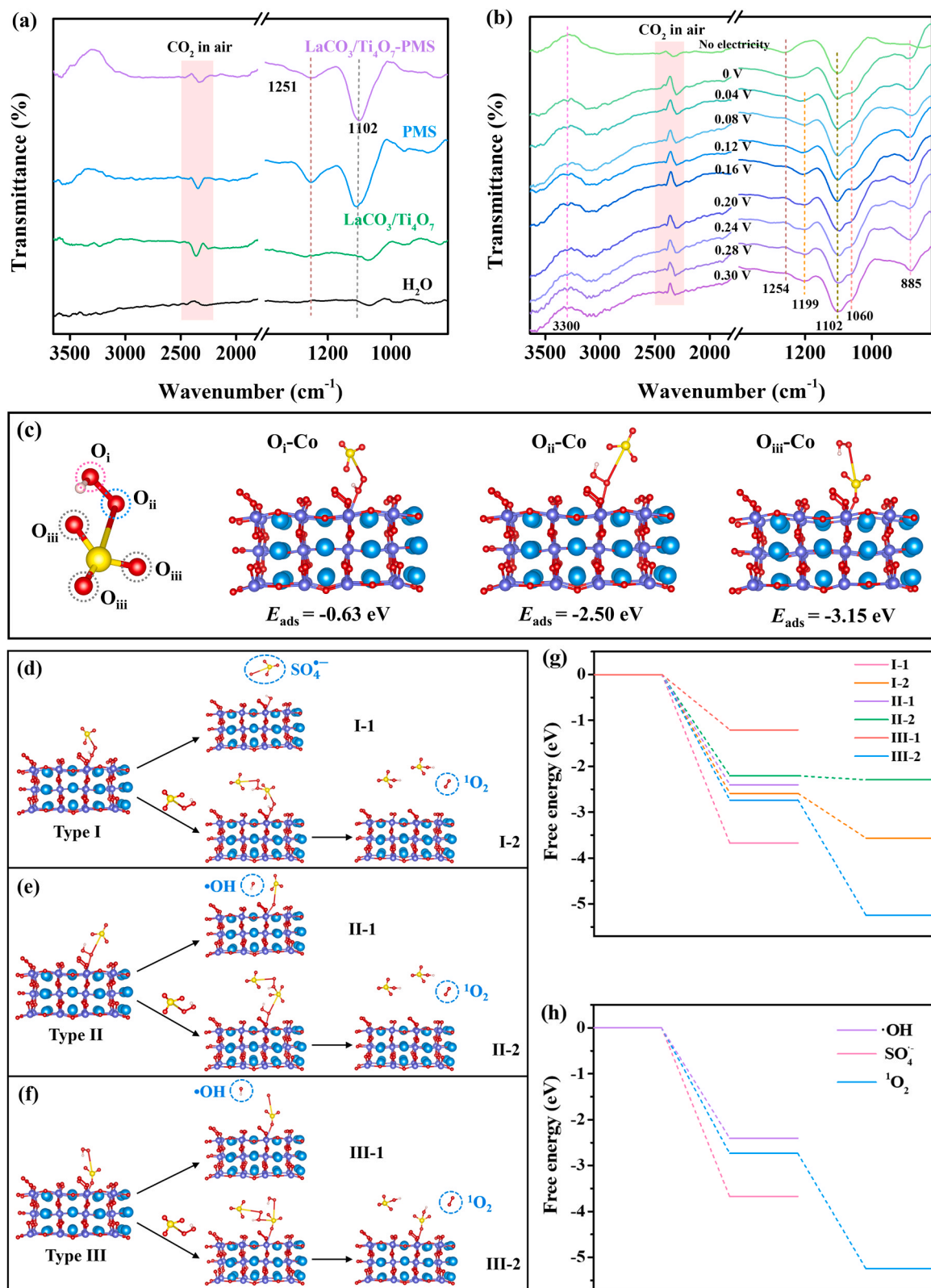
**Fig. 5.** *In-situ* FTIR spectra of PMS after adding $LaCoO_3/Ti_4O_7$ (a) and real-time spectra at a series of potentials (0–0.3 V vs Ag/AgCl) (b), the optimal adsorption configurations of Type I ($O_i$-Co), Type II ($O_{ii}$-Co), and Type III ($O_{iii}$-Co) (c), possible pathways for PMS activation via Type I (d), Type II (e) and Type III (f) adsorption configurations, the Gibbs free energy for the generation of $^\bullet$OH, $SO_4^{\bullet-}$ and $^1O_2$ in six pathways (g) and comparison of the primary route for $^\bullet$OH, $SO_4^{\bullet-}$ and $^1O_2$ (h).

was apt to be adsorbed and further activated by LaCoO$_3$ ($E_{ads}$ = −3.15 eV; Fig. S13a) rather than Ti$_4$O$_7$ ($E_{ads}$ = −0.85 eV; Fig. S13b). The La atoms at A position are responsible for stabilizing the crystal structure of LaCoO$_3$, while the Co atoms at B position are the active sites for PMS adsorption and activation [9]. It has been reported that adsorption types involving different O atoms for binding and exposure led to diverse routes of PMS activation and resultant ROS generation [41]. As depicted in Fig. 5c, PMS comprises three types of O atoms to bind the Co active site, one hydroxyl O atom (O$_i$), one peroxy O atom (O$_{ii}$), and three terminal O atoms (O$_{iii}$). The corresponding adsorption configurations are designated as Type I, Type II, and Type III, respectively. The optimal configurations for Types I, II, and III, as determined through DFT calculations, were presented in Fig. 5c, respectively. Notably, the adsorption energy of O$_{iii}$ exhibited the most negative value ($E_{ads}$ = −3.15 eV) among the three types, signifying the exceptional stability and prevalence of Type III PMS adsorption. According to different adsorption configurations, PMS can produce different ROS through different intermediates in six ways. The cleavage of peroxy bond (O$_i$-O$_{ii}$) emerged as a pivotal factor in the radical-based oxidation mechanism [41]. In Fig. 5d-f, pathway I-1 represented the pathway for generating SO$_4^{\bullet-}$, while II-1 and III-1 depicted the pathways for $\bullet$OH formation. The length of O$_i$-O$_{ii}$ bond in Type III was lower than that in Type II, supporting that $\bullet$OH was more prone to producing through the cleavage of the O$_i$-O$_{ii}$ bond in Pathway II-1 (Table S5). The Gibbs free energy (ΔG) provided compelling evidence for the PMS activation mechanism (Fig. 5g). Pathway II-1 was thermodynamically easier to happen compared to pathway III-1, also suggesting that II-1 was the primary route for generating $\bullet$OH. Pathway I-1 governed the exclusive production of SO$_4^{\bullet-}$.

Generally, the $^1$O$_2$ may be derived from several possible pathways: (i) the self-decomposition of PMS, (ii) recombination or proton-promoted disproportionation from the O$_2^{\bullet-}$ intermediate, and (iii) nucleophilic addition between active sites on the catalysts and PMS. From the results in Fig. 3a-b, PMS has extremely minimal impact on the degradation and mineralization of CBZ, illustrating the negligible role of self-decomposition of PMS for $^1$O$_2$ conversion. The quenching

experiments and EPR spectra (Fig. S9 and Fig. 4d) indicated the virtual absence of O$_2^{\bullet-}$ in the system, implying the second pathway for $^1$O$_2$ could also be disregarded. Thus, the third way from nucleophilic addition of active sites and PMS predominated the $^1$O$_2$ formation in the E-REM-PMS system. As discovered in the previous research, PMS bound to the catalyst could react with another PMS molecule to generate $^1$O$_2$ via the potential pathways I-2, II-2, and III-2 [41]. It has been reported that $^1$O$_2$ generation predominantly occurred through the interaction between O$_i$ and O$_{ii}$ from the same PMS attached to the catalyst, and the remaining HSO$_3^-$ combined with another PMS to produce two HSO$_4^-$ molecules [41]. Due to the adsorption of O$_i$ or O$_{ii}$ by LaCoO$_3$ in pathways I-2 and II-2, a higher energy requirement was necessary to break the bonds of PMS oxygen atom and metal atom to liberate the singlet O$_i$-O$_{ii}$. Pathway III-2 with fully exposed O$_i$ or O$_{ii}$ presented the lowest energy barriers among the three pathways, which was more prone to be activated into $^1$O$_2$ (Fig. 5g). The cleavage of S-O$_{ii}$ bond was crucial for the formation of $^1$O$_2$. As shown in Table S5, the relative elongation value of S-O$_{ii}$ bond was significantly larger than that of O$_i$-O$_{ii}$ bond in Type III, indicating a preference for the generation of $^1$O$_2$ over $\bullet$OH. Furthermore, the length of S-O$_{ii}$ bond in the Type III exceeded those in Types I and II, providing additional evidence for the predominance of pathway III-2 in $^1$O$_2$ generation (Table S5). However, the elongation values of S-O$_{ii}$ bond were shorter than those of the O$_i$-O$_{ii}$ bond in Types I and II, suggesting that Types I and II were more conducive to the cleavage of O$_i$-O$_{ii}$ and generation of SO$_4^{\bullet-}$ and $\bullet$OH. Hence, I-1, II-1 and III-2 were the primary mechanisms governing the formation of SO$_4^{\bullet-}$, $\bullet$OH and $^1$O$_2$, respectively. Based on the comparative analysis in Fig. 5h, III-2 is the most likely to occur, followed by I-1, and lastly II-1. This finding established the sequence of ROS generation as $^1$O$_2$, SO$_4^{\bullet-}$ and $\bullet$OH, in accordance with the experiments results.

Therefore, the activation mechanism in the E-REM-PMS system was proposed in Fig. 6. Initially, PMS (HSO$_5^-$) substituted some surface −OH and bonded with the Co atoms of LaCoO$_3$ to form three types of metastable complexes named as Co$^{2+}$−(HO)OSO$_3^-$ (O$_i$ site), Co$^{2+}$−O(HO)SO$_3^-$ (O$_{ii}$ site) and (HO)OSO$_3^-$−Co$^{2+}$ (O$_{iii}$ site) (Eq. (1)).
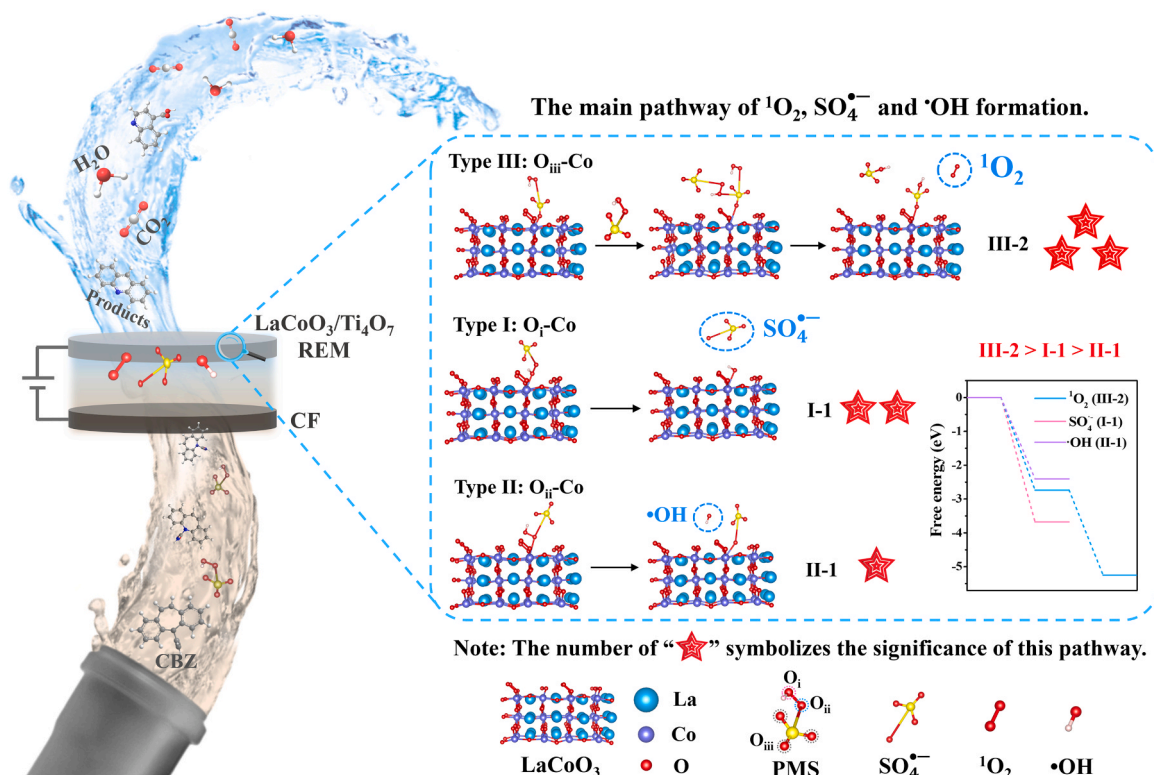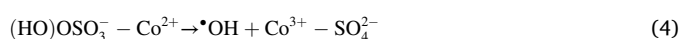


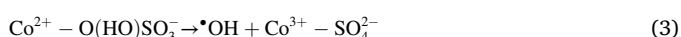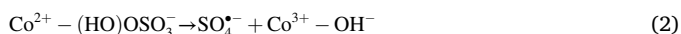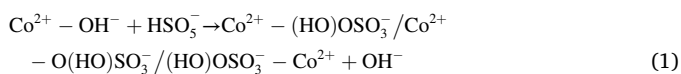**Fig. 6.** Schematic of the proposed mechanism for CBZ degradation in the E-REM-PMS system.

Subsequently, the metastable $Co^{2+}-(HO)OSO_3^-$ species rapidly decomposed into $Co^{3+}-OH^-$ and $SO_4^{\bullet-}$ from pathway I-1 as Eq. (2) [42]. $^\bullet OH$ derived from the direct decomposition at $O_{ii}$ site in $Co^{2+}-O(HO)SO_3^-$ and $(HO)OSO_3^--Co^{2+}$ as depicted in pathway II-1 and III-1 (Eqs. (3)-(4)). The reaction pathway I-2, II-2 and III-2 between three types of metastable complexes and another $HSO_5^-$ contributed to the production of $^1O_2$ (Eqs. (5)-(7)). Due to the results of DFT calculation, pathway III-2, I-1 and II-1 dominated the formation of $^1O_2$, $SO_4^{\bullet-}$ and $^\bullet OH$, respectively. Theoretical calculation and experiments result consistently demonstrated that $^1O_2$ assumed a leading role in this system, followed by $SO_4^{\bullet-}$ and $^\bullet OH$.

$$Co^{2+}-OH^- + HSO_5^- \rightarrow Co^{2+}-(HO)OSO_3^-/Co^{2+} \\ -O(HO)SO_3^-/(HO)OSO_3^--Co^{2+} + OH^- \tag{1}$$

$$Co^{2+}-(HO)OSO_3^- \rightarrow SO_4^{\bullet-} + Co^{3+}-OH^- \tag{2}$$

$$Co^{2+}-O(HO)SO_3^- \rightarrow {}^\bullet OH + Co^{3+}-SO_4^{2-} \tag{3}$$

$$(HO)OSO_3^--Co^{2+} \rightarrow {}^\bullet OH + Co^{3+}-SO_4^{2-} \tag{4}$$

$$Co^{2+}-(HO)OSO_3^- + HSO_5^- \rightarrow {}^1O_2 + Co^{2+} + 2HSO_4^- \tag{5}$$

$$Co^{2+}-O(HO)SO_3^- + HSO_5^- \rightarrow {}^1O_2 + Co^{2+} + 2HSO_4^- \tag{6}$$

$$(HO)OSO_3^--Co^{2+} + HSO_5^- \rightarrow {}^1O_2 + (HO)OSO_3^--Co^{2+} + HSO_4^- \tag{7}$$
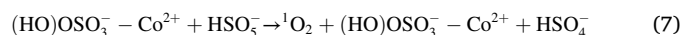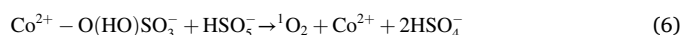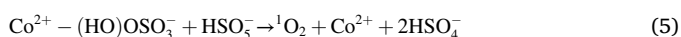
### 3.4. Degradation pathway and toxicity evaluation

It has been reported that the HOMO (Highest Occupied Molecular Orbital) of CBZ molecule is principally located on both sides of C=C, where is more willing to be attacked by electrophiles [43]. The active sites of the olefin double bond with the highest Fukui index value are most likely to be attacked by electrophilic species. Therefore, unsaturated bonds and carbon atoms on the benzene ring were prone to be cleaved by $^1O_2$ and $SO_4^{\bullet-}$ [44,45]. As clarified in Fig. 7a, the double bonds on the central heterocyclic ring of CBZ olefin were converted to alcohols, ketones and aldehydes, while the external two aromatic rings remained intact in all products (Table S6). CBZ was easily attacked by $^1O_2$ and $SO_4^{\bullet-}$ and epoxidized into a possible degradation product P1 (10,11-epoxycarbamazepine, $m/z=253$). Three pathways were speculated to exist in the further degradation of P253. First, both intramolecular cyclisation and amine/acrylamide cleavage could occur simultaneously, leading to the formation of P2 ($m/z=210$). P3
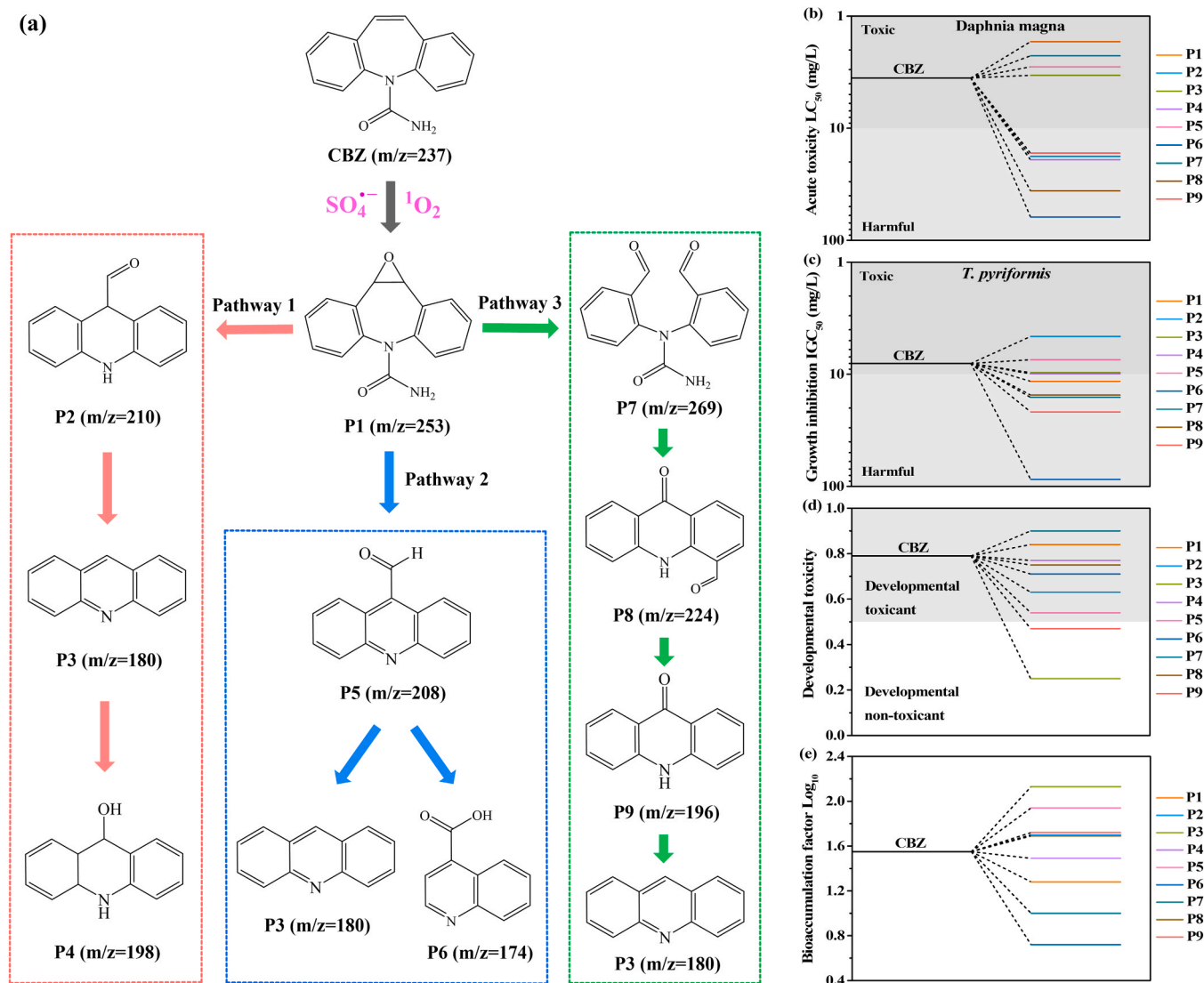


**Fig. 7.** Proposed CBZ degradation pathways in the E-REM-PMS system (a), Daphnia magna LC$_{50}$ (48 h) (b), *T. pyriformis* IGC$_{50}$ (48 h) (c), developmental toxicity (d) and bioconcentration factor Log$_{10}$ (e) of CBZ and its possible degradation intermediates.

($m/z$=180) generated after losing the carbonyl group from P2 and then oxidized by $^1O_2$ to yield P4 ($m/z$=198).[46] In the second pathway, P1 intermediate could be oxidized and shrunk to generate P5 ($m/z$=208) through oxidation ring, and subsequently P5 might undergo further oxidation to yield smaller molecules P3 ($m/z$=180) and P6 ($m/z$=174) [47]. For the third pathway, the C-C bond of P1 might be cleaved to form the dialdehyde product P7 ($m/z$=269). P7 was converted to P8 ($m/z$= 224) due to benzene ring on P7 could spin around the C-N bond and amine/acylamido cleavage [37]. The intermediate P8 presumably removed aldehyde group to form P9 ($m/z$=196), and P9 was further oxidized into P3 ($m/z$=180) through incision [48]. Ultimately, the intermediates were attacked by ROS, resulting in ring cleavage and the formation of smaller molecules or $CO_2$.

The Toxicity Estimation Software Tool (T.E.S.T) based on the quantitative structure-activity relationship (QSAR) was employed to evaluate the degradation intermediates of CBZ in the E-REM-PMS system. As depicted in Fig. 7 and Table S7, acute toxicity $LC_{50}$, growth inhibition $IGC_{50}$, developmental toxicity and bioconcentration factor of CBZ and possible intermediates were predicted. The Daphnia magna $LC_{50}$ (48 h) and *T. pyriformis* $IGC_{50}$ (48 h) of CBZ were categorized as "Toxic" pollution, whereas most of intermediates exhibited higher $LC_{50}$ and $IGC_{50}$ values than 10 mg/L and turned into "Harmful" pollution (Fig. 7b-c). Moreover, most of the degradation products showed less developmental toxicity than CBZ except P1 and P7 which displayed slightly higher toxicity than CBZ, with P3 and P9 even reaching "non-toxicant" (Fig. 7d). The main final products (P3, P4 and P6) in the three pathways were less toxic than CBZ despite high toxicity of partial intermediates, indicating that the acute and developmental toxicity of CBZ were effectively diminished after degradation. The bioconcentration factors of some intermediates were higher than CBZ, but no bio-accumulation or genotoxicity was discerned for the evaluated degradation intermediates (Fig. 7e) [49]. The overall prediction results demonstrated that the environmental risks of CBZ could be mitigated

during degradation process in E-REM-PMS system.

### 3.5. Potential environmental applications

#### 3.5.1. Broad pH suitability

The pH applicability, versatility, stability and interference immunity are the key indexes to estimate the application prospects in practical wastewater treatment. To verify the pH suitability of $LaCoO_3/Ti_4O_7$ REM, the influence of initial pH values (3−10) on CBZ removal was conducted. In Fig. 8a, the CBZ removal maintained above 85% over the p H range 4−10 in the continuous flow mode, while regrettably weaker performance (60%) presented at pH 3. It can be clearly observed that the reaction process was hindered under strong acidic (pH 3–4) and strong alkaline conditions (pH 10). The results could be elucidated from the following aspects: (i) Under strong acid conditions, massive $H^+$ in solution quenched the free radicals ($SO_4^{\bullet-}$ and $^{\bullet}OH$) formed in the system (Eqs. (8)-(9)), weakening the ability of the system to degrade CBZ. Additionally, the stabilizing effect of $H^+$ on $HSO_5^-$ species is not conducive to activate PMS to remove pollutants in the superacid conditions [50]. (ii) $HSO_5^-$ is the primary PMS species in acidic and neutral solutions ($pK_{a1} < 0$ and $pK_{a2} = 9.4$), whereas $SO_5^{2-}$ with weaker activity mainly existed at a strongly alkaline condition [51]. Therefore, the slight decrease of CBZ degradation at pH 10 might be caused by the relatively poor catalytic activity of $SO_5^{2-}$.

$$H^+ + SO_4^{\bullet-} + e^- \rightarrow HSO_4^- \tag{8}$$

$$H^+ + {}^{\bullet}OH + e^- \rightarrow H_2O \tag{9}$$
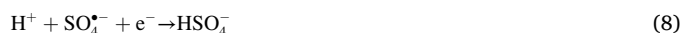
The leakages of La and Co were tested to evaluate whether E-REM-PMS system throwed a potential risk to the environment. As shown in Fig. 8b, the leaching concentrations of La and Co gradually decreased with the initial pH increasing. The metal leakages were relatively high in
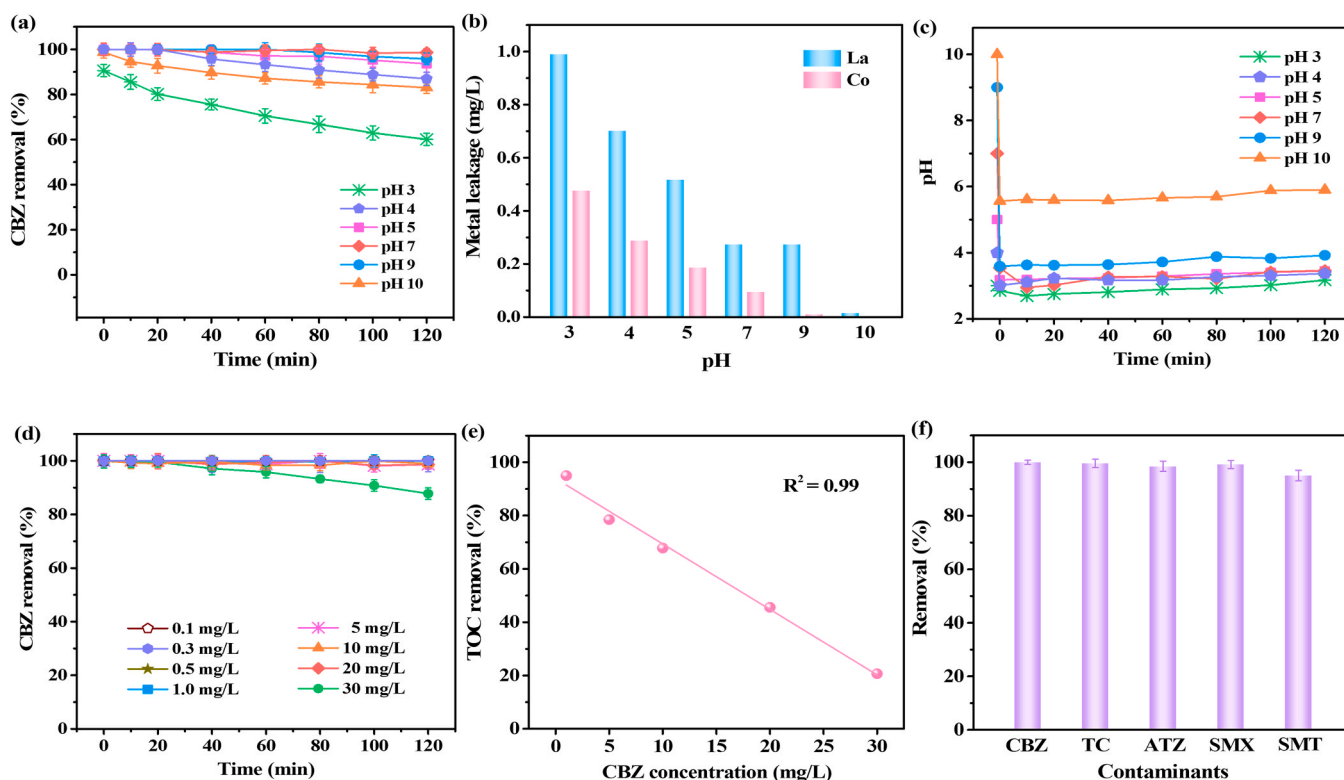


**Fig. 8.** The effect of initial pH on CBZ elimination in the E-REM-PMS system (a), the leakage of La and Co under different pH (b), pH evolution after the reaction under different initial pH (c), CBZ removal under the initial concentration of 0.1–30 mg/L (d), the TOC mineralization at different concentrations of CBZ (e) and the versatility of the E-REM-PMS system for various pharmaceuticals (f). Reaction conditions: [PMS] = 2 mM, flow rate = 7.5 mL/min, current density = 0.5 mA/cm².

acidic condition, and especially at pH 3, the leaching La and Co reached 0.99 mg/L and 0.48 mg/L respectively. The increased leaching might arise from acidic conditions that disrupt the structure of a fraction of $LaCoO_3$ perovskite. Compared to Co ions, the higher release of La is primarily attributed to its larger relative atomic mass. More metal loss in the catalyst might lead to weaker contaminant removal at pH=3. The pH evolution after the reaction under different initial pH was monitored and displayed in Fig. 8c. When the reaction began, the pH of the continuous-flow effluent immediately dropped and remained around 3 due to the formation of strong acidic byproducts during the deep mineralization. And the lower the initial pH, the lower the post-reaction pH and the more metal leakage. However, higher metal leakage under pH 3 did not lead to better CBZ removal, indicating that the E-REM-PMS system was mainly driven by the heterogeneous reaction of the $LaCoO_3/Ti_4O_7$ REM rather than the homogeneous reaction. The adaptability in wide pH range (4−10) of E-REM-PMS system showed great potentials to the treatments of wastewater with different pH levels.

### 3.5.2. Versatility

The versatility of E-REM-PMS system determines the application potential in the actual wastewater decontamination, which was estimated by different CBZ concentrations and various micropollutants. As displayed in Fig. 8d, approximate 100% CBZ could be removed under the initial concentration of 0.1–20 mg/L. When the CBZ concentration increased to 30 mg/L, the instantaneous removal of CBZ reduced to 85% as the reaction time extended to 120 min. It can be speculated that high concentration would cause partial CBZ to adsorb and occupy the active site of $LaCoO_3/Ti_4O_7$ REM, lowering the PMS activation ability of anode REM. TOC mineralization in the E-REM-PMS system was negatively correlated with CBZ concentration (Fig. 8e). As the CBZ dosage decreased from 30 to 1 mg/L, the TOC removal gradually enhanced from 21% to 95%. Thus it can be conjectured that the system showed great prospect for attaining nearly 100% mineralization when the

concentration of CBZ falls below 1 mg/L. The mineralization of 10 mg/L CBZ in the E-REM-PMS system reached 67.8%, which was higher than that of 10 mg/L SMX in the advanced $Fe$-$SA/Mo_2TiC_2T_x/PMS$ system (58.8%) [7]. The outstanding removal of CBZ and TOC illustrated significant advantages of E-REM-PMS system, enabling highly efficient and environmentally decontamination.

Various pharmaceuticals (20 mg/L) including TC, SMT, SMX and ATZ were selected to explore the versatility of $LaCoO_3/Ti_4O_7$ REM. In Fig. 8f, CBZ, TC and SMX could be degraded above 98%, and the elimination of SMT and ATZ also reached more than 90%. The E-REM-PMS system exhibited outstanding removal capacity for different contaminants, which is conducive to the treatment of practical wastewater with combined pollution. Besides, inorganic ions and natural organic matters (NOMs) were chosen to evaluate the interference immunity of E-REM-PMS system. In Fig. 9a, $SO_4^{2-}$, $Cl^-$, $NO_3^-$, HA and FA hardly disturbed the removal of CBZ, while $PO_4^{3-}$ restrained CBZ removal by 15%, which might be caused by the competitive effect between $PO_4^{3-}$ and reactive species [52]. $CO_3^{2-}$ showed gradual inhibition to the CBZ degradation, which could be ascribed to the formation of carbonate radical ($CO_3^{\bullet-}$) from Eqs. (10)-(11) with much less reactive and more selective than $SO_4^{\bullet-}$ and $^\bullet OH$ [53]. The versatility and anti-interference performance showed good potential of E-REM-PMS system for water treatment.

$$CO_3^{2-} + SO_4^{\bullet-} \rightarrow CO_3^{\bullet-} + SO_4^{2-} \tag{10}$$

$$CO_3^{2-} + {}^\bullet OH \rightarrow CO_3^{\bullet-} + OH^- \tag{11}$$

### 3.5.3. Reusability

Except for pH applicability and versatility, the stability and durability of REM are also crucial. In Fig. 9b, the $LaCoO_3/Ti_4O_7$ REM possessed a satisfactory reusability in 20 consecutive experiments. Reasonable stability was achieved in the first 15 cycles, with the degradation efficiency of CBZ showing slight fluctuation. After 15
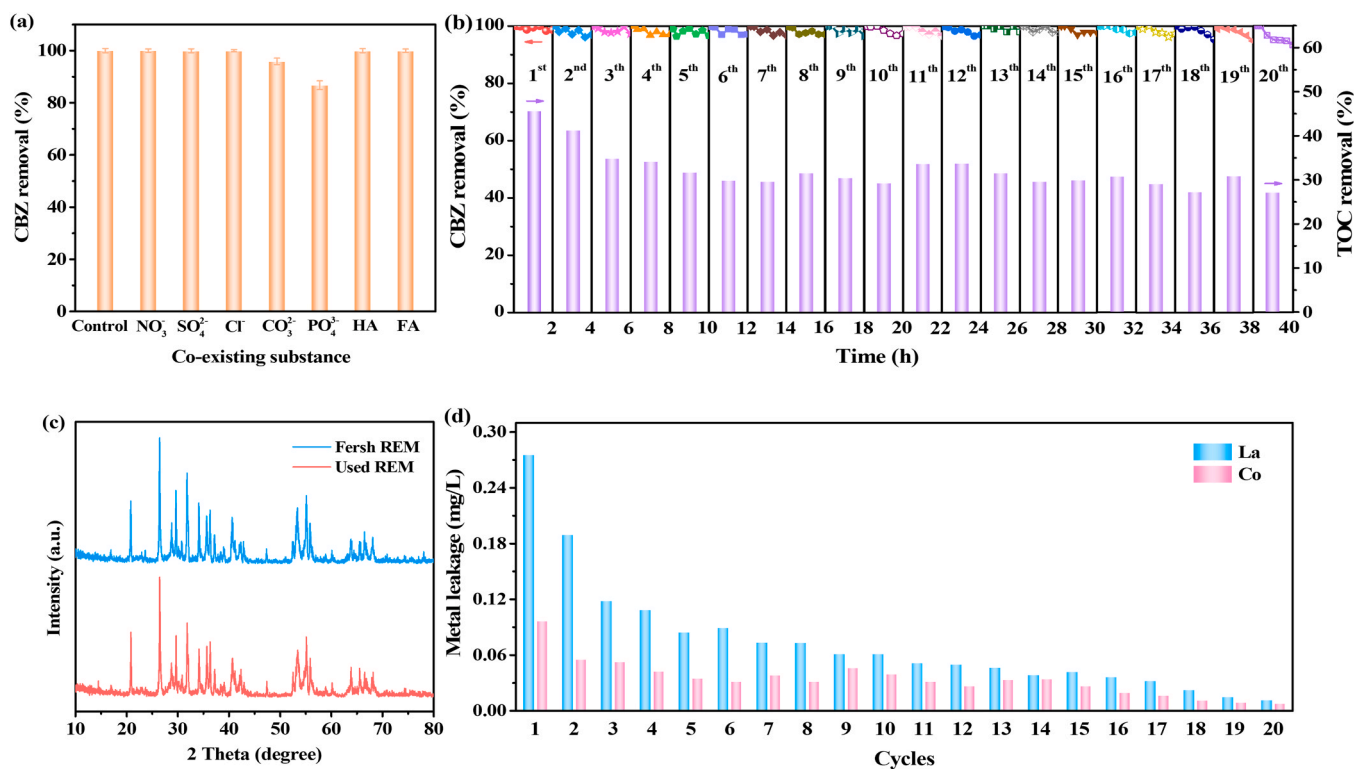


**Fig. 9.** The effects of co-existing substances in the E-REM-PMS system (a), CBZ and TOC removal in 20 consecutive experiments (b), XRD patterns of $LaCoO_3/Ti_4O_7$ before or after 20 cycles (c) and the leaching La and Co in the E-REM-PMS system in 20 consecutive experiments (d). Reaction conditions: [CBZ] = 20 mg/L, [PMS] = 2 mM, current density = 0.5 mA/cm$^2$, flow rate = 7.5 mL/min, influent solution pH = 7.

cycles, the CBZ removal in the E-REM-PMS system exhibited a small decrease, which declined to 93.3% in the 20th cycle. The TOC mineralization reached 45.6% and 41.1% in the first and second cycle, then undulating around 30% in the following cycles. The XRD patterns of $LaCoO_3/Ti_4O_7$ before and after reusing 20 times displayed no significant difference (Fig. 9c). Besides, the concentrations of leaching La and Co reduced with the increasing cycles in 20 consecutive rounds (Fig. 9d). La leakage was higher in the first 5 cycles, and then lower than 0.2 mg/L in the subsequent 15 cycles. Cobalt dissolution was generally low, less than 0.1 mg/L after the 4th round and even below 0.05 mg/L after the 9th round. The initial higher leaching in the first few cycles may be attributed to the initially unstable structure of the REM. As the reaction progresses over five cycles, the electrode gradually stabilizes, resulting in a stabilized leaching of metal ions. As calculated, the total La and Co leakages in 20 cycles were 1.33 mg and 0.62 mg, respectively. Each 0.15 wt% $LaCoO_3/Ti_4O_7$ contains 15 mg $LaCoO_3$, comprising 8.5 mg of La and 3.6 mg of Co. Hence, the leached amounts of La and Co accounted for approximately 15.6% and 17.2% of the fresh $LaCoO_3/Ti_4O_7$. The fewer amount of metal leaching would not impact the sustained performance of the $LaCoO_3/Ti_4O_7$ REM, which maintained 93.3% CBZ removal even after 20 reuses. The concentration of residual homogeneous Co ions in the solution remains below the allowable wastewater discharge standard, as stipulated by the Emission Standard of Pollutants for Copper, Nickel, Cobalt Industry of China (Co ≤1 mg/L) [54]. At the end of their operational lifespan, REMs can be easily recovered and processed, thereby minimizing their environmental impact. These results showed the $LaCoO_3/Ti_4O_7$ REM has a high corrosion resistance and a good stability under anodic conditions [55]. The minimal metal leaching and convenient recovery of REM substantiated the safety and potential of employing $LaCoO_3/Ti_4O_7$ REM. The outstanding reusability for 20 cycles indicated the huge potential of $LaCoO_3/Ti_4O_7$ anode REM in practical application, superior to the advanced research of PMS activation via $Fe-SA/Mo_2TiC_2T_x$ electroactive filter with ~86% SMX degradation after five consecutive running cycles

[7]. The exceptional stability of $LaCoO_3/Ti_4O_7$ REM might be attributed to the physical stability and chemical inertness of the inherent structures of both $LaCoO_3$ and $Ti_4O_7$, which avoided being affected by reactants or reaction conditions. In summary, the E-REM-PMS system has shown excellent application prospects in simulated wastewater.

### 3.6. Actual pharmaceutical wastewater treatment

To explore the potential of $LaCoO_3/Ti_4O_7$ REM in practical water matrix, continuous experiment (10 h) was conducted in the pharmaceutical wastewater. The quality parameters of pharmaceutical wastewater were listed in Table S8. It has been reported that the concentration of CBZ in the actual pharmaceutical wastewater is 0.77–7.5 μg/L in hospital effluents of different countries [56]. And the mean concentrations of CBZ were 60.58, 93.19 and 132 μg/L in wastewater treatment plants of the Bizerte, Jendouba and Tunis, respectively [57]. Hence, environmentally relevant concentrations (0.1 mg/L or 0.5 mg/L) of CBZ were added into the pharmaceutical wastewater to investigate the removal performance of the E-REM-PMS system in practical application. As shown in Fig. 10a, both 0.1 mg/L and 0.5 mg/L CBZ could be removed ~100 % sustaining 10 h operations in the pharmaceutical wastewater at a high water flux of 642.86 $L/m^2$·h. The TOC mineralization of pharmaceutical wastewater could be maintained at a range of 60 %-70 % during the continuous reaction for 10 h, corresponding to approximately 35–42 mg/L of TOC removal. As calculated, the total treatment capacity of pharmaceutical wastewater can reach 4.5 L within a 10-hour duration. The continuous and stable removal of CBZ and TOC of $LaCoO_3/Ti_4O_7$ REM confirmed that the E-REM-PMS system possessed superior catalytic activity and exceptional durability. Different from homogeneous and heterogeneous processes, the $LaCoO_3/Ti_4O_7$ REM also possessed the advantage of convenient recovery. Moreover, the elimination of all organic substances in pharmaceutical wastewater was assessed through three-dimensional excitation and emission matrix (3D-EEM). As depicted in Fig. 10b and 10d, the original pharmaceutical
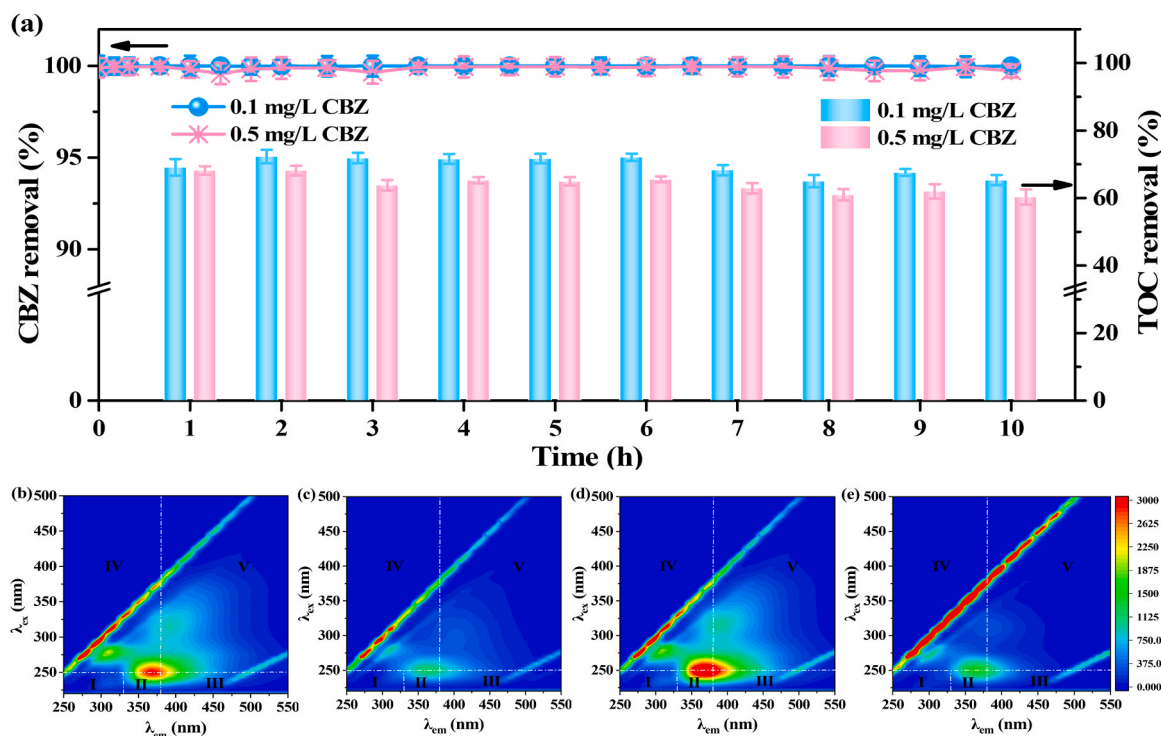


**Fig. 10.** CBZ and TOC removal in pharmaceutical wastewater by the E-REM-PMS system (with the addition of 0.1 mg/L and 0.5 mg/L CBZ) (a), 3D-EEM fluorescence spectra of pharmaceutical wastewater with the addition of 0.1 mg/L CBZ before (b) and after treatment (c), 3D-EEM results of pharmaceutical wastewater with the addition of 0.5 mg/L CBZ before (d) and after treatment (e). Reaction conditions: [PMS] = 2 mM, flow rate = 7.5 mL/min, influent solution pH = unadjusted, current density = 0.5 $mA/cm^2$.

wastewater with 0.1 mg/L or 0.5 mg/L CBZ adding contained five parts of fluorescent substances, indicating tyrosine aromatic proteins (I), tryptophan aromatic proteins (II), FA-like (III), soluble microbial byproduct (IV) and HA-like substances (V). The pharmaceutical wastewater with 0.5 mg/L CBZ exhibited a higher initial fluorescence intensity compared to that with 0.1 mg/L CBZ. The fluorescence intensity of both wastewater samples was significantly reduced after treatment, indicating that the E-REM-PMS system could mineralize and decompose macromolecular organics into small molecular organics (Fig. 10c and 10e). The EEM results substantiated the efficient decontamination wastewater performance of this system for real pharmaceutical wastewater. The ultrafast wastewater decontamination ($k = 39.69\ min^{-1}$), high water flux (642.86 L/m$^2$·h), extremely low energy consumption ($0.01 \pm 0.001$ kWh/m$^3$·order) and convenient recovery made it a highly promising solution for practical applications in wastewater treatment.

## 4. Conclusion

This study highly enhanced the efficiency and overcame the limitations of catalyst recovery, reusability and poor performance in actual wastewater treatment via designing a LaCoO$_3$/Ti$_4$O$_7$ REM to activate PMS by a flow-through mode. The E-REM-PMS system successfully achieved a remarkable rate constant, high water flux and long-term test in pharmaceutical wastewater at a very low energy consumption. The enhanced CBZ degradation kinetics could be attributed to the synergistic effects of the LaCoO$_3$/T$_4$O$_7$ REM, electric field and PMS. The reaction mechanism including leading species and generation pathways of ROS were confirmed via DFT calculations and *in-situ* FTIR spectroscopy. The desirable reusability, interference immunity of LaCoO$_3$/T$_4$O$_7$ REM and versatility for various contaminants suggested a great potential for practical applications. The sustained and stable performance of the E-REM-PMS process in the long-term treatment of actual pharmaceutical wastewater affirmed its viability as an environmentally friendly strategy for wastewater management. We envision that this work will lay a scientific foundation for the ultra-efficient and low-cost decontamination of wastewater.

## CRediT authorship contribution statement

**Huizhong Wu:** Software, Methodology, Investigation. **Minghua Zhou:** Writing – review & editing, Supervision, Project administration, Formal analysis, Conceptualization. **Xuechun Wang:** Validation, Software. **Jinxin Xie:** Investigation, Formal analysis. **Jiana Jing:** Writing – original draft, Software, Methodology, Investigation, Conceptualization.

## Declaration of Competing Interest

The authors declare that they have no known competing financial interests or personal relationships that could have appeared to influence the work reported in this paper.

## Data Availability

Data will be made available on request.

## Acknowledgements

## Appendix A. Supporting information

## References

[1] Z. Xiao, B. Yang, X. Feng, Z. Liao, H. Shi, W. Jiang, C. Wang, N. Ren, Density functional theory and machine learning-based quantitative structure-activity relationship models enabling prediction of contaminant degradation performance with heterogeneous peroxymonosulfate treatments, Environ. Sci. Technol. 57 (2023) 3951–3961.

[2] J. Lee, U. von Gunten, J.H. Kim, Persulfate-based advanced oxidation: critical assessment of opportunities and roadblocks, Environ. Sci. Technol. 54 (2020) 3064–3081.

[3] Z. Xu, Y. Wu, X. Wang, Q. Ji, T. Li, H. He, H. Song, S. Yang, S. Li, S. Yan, L. Zhang, Z. Zou, Identifying the role of oxygen vacancy on cobalt-based perovskites towards peroxymonosulfate activation for efficient iohexol degradation, Appl. Catal. B Environ. 319 (2022) 121901.

[4] B.C. Hodges, E.L. Cates, J.H. Kim, Challenges and prospects of advanced oxidation water treatment processes using catalytic nanomaterials, Nat. Nanotechnol. 13 (2018) 642–650.

[5] X. Mi, P. Wang, S. Xu, S. Su, H. Zhong, H. Wang, Y. Li, S. Zhan, Almost 100 % peroxymonosulfate conversion to singlet oxygen on single-atom CoN$_{2+2}$ sites, Angew. Chem. Int. Ed. Engl. 60 (2021) 4588–4593.

[6] G.P. Anipsitakis, D.D. Dionysiou, Radical generation by the interaction of transition metals with common oxidants, Environ. Sci. Technol. 38 (2004) 3705–3712.

[7] L. Jin, S. You, N. Ren, B. Ding, Y. Liu, Mo vacancy-mediated activation of peroxymonosulfate for ultrafast micropollutant removal using an electrified MXene filter functionalized with Fe single atoms, Environ. Sci. Technol. 56 (2022) 11750–11759.

[8] K. Wang, C. Han, F. Li, Y. Liu, Z. Shao, L. Liu, S. Wang, S. Liu, An intrinsic descriptor of perovskite cobaltites for catalytic peroxymonosulfate activation toward water remediation, Appl. Catal. B: Environ. 320 (2023) 121990.

[9] M.A. Pena, J.L.G. Fierro, Chemical structures and performance of perovskite oxides, Chem. Rev. 101 (2001) 1981–2017.

[10] S.B. Hammouda, F. Zhao, Z. Safaei, V. Srivastava, D. Lakshmi Ramasamy, S. Iftekhar, S. kalliola, M. Sillanpää, Degradation and mineralization of phenol in aqueous medium by heterogeneous monopersulfate activation on nanostructured cobalt based-perovskite catalysts ACoO$_3$ (A = La, Ba, Sr and Ce): characterization, kinetics and mechanism study, Appl. Catal. B Environ. 215 (2017) 60–73.

[11] D. Manos, F. Papadopoulou, A. Margellou, D. Petrakis, I. Konstantinou, Heterogeneous activation of persulfate by LaMO$_3$ (M=Co, Fe, Cu, Mn, Ni) perovskite catalysts for the degradation of organic compounds, Catalysts 12 (2022) 187.

[12] X. Wang, J. Jing, M. Zhou, R. Dewil, Recent advances in H$_2$O$_2$-based advanced oxidation processes for removal of antibiotics from wastewater, Chin. Chem. Lett. 34 (2023) 107621.

[13] C. Trellu, B.P. Chaplin, C. Coetsier, R. Esmilaire, S. Cerneaux, C. Causserand, M. Cretin, Electro-oxidation of organic pollutants by reactive electrochemical membranes, Chemosphere 208 (2018) 159–175.

[14] K. Yang, H. Lin, X. Feng, J. Jiang, J. Ma, Z. Yang, Energy-efficient removal of trace antibiotics from low-conductivity water using a Ti$_4$O$_7$ reactive electrochemical ceramic membrane: matrix effects and implications for byproduct formation, Water Res. 224 (2022) 119047.

[15] B.P. Chaplin, The prospect of electrochemical technologies advancing worldwide water treatment, Acc. Chem. Res. 52 (2019) 596–604.

[16] S. Almassi, Z. Li, W. Xu, C. Pu, T. Zeng, B.P. Chaplin, Simultaneous adsorption and electrochemical reduction of N-nitrosodimethylamine using carbon-Ti$_4$O$_7$ composite reactive electrochemical membranes, Environ. Sci. Technol. 53 (2019) 928–937.

[17] M. Li, Y.T. Jin, J.F. Yan, Z. Liu, N.X. Feng, W. Han, L.W. Huang, Q.K. Li, K.L. Yeung, S.Q. Zhou, C.H. Mo, Exploration of perfluorooctane sulfonate degradation properties and mechanism via electron-transfer dominated radical process, Water Res. 215 (2022) 118259.

[18] P. Gayen, C. Chen, J.T. Abiade, B.P. Chaplin, Electrochemical oxidation of atrazine and clothianidin on Bi-doped SnO$_2$-Ti$_n$O$_{2n-1}$ electrocatalytic reactive electrochemical membranes, Environ. Sci. Technol. 52 (2018) 12675–12684.

[19] K. He, W. Li, L. Tang, L. Chen, G. Wang, Q. Liu, X. Xin, C. Yang, Z. Wang, S. Lv, D. Xing, Insight into the design of a Ti$_3$C$_2$ MXene/Ti$_4$O$_7$ composite ceramic membrane boosts the electrocatalytic activity for 1,4-dioxane electro-oxidation, Appl. Catal. B: Environ. 338 (2023) 123077.

[20] L. Jin, S. You, X. Duan, Y. Yao, J. Yang, Y. Liu, Peroxymonosulfate activation by Fe$_3$O$_4$-MnO$_2$/CNT nanohybrid electroactive filter towards ultrafast micropollutants decontamination: performance and mechanism, J. Hazard. Mater. 423 (2022) 127111.

[21] L. Jin, S. You, Y. Yao, H. Chen, Y. Wang, Y. Liu, An electroactive single-atom copper anchored MXene nanohybrid filter for ultrafast water decontamination, J. Mater. Chem. A 9 (2021) 25964–25973.

[22] S. Li, M. Zhou, H. Wu, G. Song, J. Jing, N. Meng, W. Wang, High-efficiency degradation of carbamazepine by the synergistic electro-activation and bimetals (FeCo@NC) catalytic-activation of peroxymonosulfate, Appl. Catal. B: Environ. 338 (2023) 123064.

[23] Y. Yuan, M. Nie, C. Yan, L. Wu, W. Dong, M. Ding, P. Wang, Solar light promoted degradation of bisphenol s in carbonate/peroxymonosulfate system through accelerating singlet oxygen generation, Chem. Eng. J. 452 (2023).

[24] Y. Gao, S. Liang, B. Liu, C. Jiang, C. Xu, X. Zhang, P. Liang, M. Elimelech, X. Huang, Subtle tuning of nanodefects actuates highly efficient electrocatalytic oxidation, Nat. Commun. 14 (2023) 2059.

[25] P. Yang, Y. Long, W. Huang, D. Liu, Single-atom copper embedded in two-dimensional MXene toward peroxymonosulfate activation to generate singlet oxygen with nearly 100 % selectivity for enhanced Fenton-like reactions, Appl. Catal. B Environ. 324 (2023) 122245.

[26] X. Wang, H. Wang, F. Li, X. Hu, Z. Xie, T. Hua, Activation of peroxymonosulfate in an electrochemical filter by $MnFe_2O_4$-rGO electro-assisted catalytic membrane for the degradation of oxytetracycline, J. Environ. Chem. Eng. 10 (2022) 107008.

[27] W. Li, R. Xiao, H. Lin, K. Yang, W. Li, K. He, L.H. Yang, M. Pu, M. Li, S. Lv, Electro-activation of peroxymonosulfate by a graphene oxide/iron oxide nanoparticle-doped $Ti_4O_7$ ceramic membrane: mechanism of singlet oxygen generation in the removal of 1,4-dioxane, J. Hazard. Mater. 424 (2022) 127342.

[28] Z. Zhao, W. Zheng, L. Jin, S. Zhang, S. You, Y. Liu, Effective peroxymonosulfate activation using electrified nanohybrid filter towards one-step decontamination of roxarsone: performance and mechanism, J. Environ. Chem. Eng. 10 (2022) 108643.

[29] J. Zhang, C. Yu, L. Xu, Z. Zhao, D. Wu, Electro-enhanced metal-free peroxymonosulfate activator coupled with membrane-assisted process for simultaneous Ni-EDTA decomplexation and Ni ions recovery, Chemosphere 338 (2023) 139447.

[30] Q. Xu, Y. Liu, Y. Wang, Y. Song, C. Zhao, L. Han, Synergistic oxidation-filtration process of electroactive peroxydisulfate with a cathodic composite CNT-PPy/PVDF ultrafiltration membrane, Water Res. 210 (2022) 117971.

[31] Y. Zhao, M. Sun, Y. Zhao, L. Wang, D. Lu, J. Ma, Electrified ceramic membrane actuates non-radical mediated peroxymonosulfate activation for highly efficient water decontamination, Water Res. 225 (2022) 119140.

[32] Y. Zhang, X. Chen, C. Liang, L. Yin, Y. Yang, Reconstructing the coordination environment of single atomic Fe-catalysts for boosting the Fenton-like degradation activities, Appl. Catal. B Environ. 315 (2022) 121536.

[33] X. Yu, H. Liu, Y. Huang, C. Li, L. Kuang, J. Zhong, S. Zhu, Y. Gou, Y. Wang, Y. Zhang, G. Shan, Z. Lv, S. Zhang, L. Zhu, A green edge-hosted zinc single-site heterogeneous catalyst for superior Fenton-like activity, Proc. Natl. Acad. Sci. U.S. A. 120 (2023) e2221228120.

[34] F.E. Scully Jr., J. Hoigné, Rate constants for reactions of singlet oxygen with phenols and other compounds in water, Chemosphere 16 (1987) 681–694.

[35] M.M. Dong, R. Trenholm, F.L. Rosario-Ortiz, Photochemical degradation of atenolol, carbamazepine, meprobamate, phenytoin and primidone in wastewater effluents, J. Hazard. Mater. 282 (2015) 216–223.

[36] B. Zhang, X. Li, K. Akiyama, P.A. Bingham, S. Kubuki, Elucidating the mechanistic origin of a spin state-dependent $FeN_x$-C catalyst toward organic contaminant oxidation via peroxymonosulfate activation, Environ. Sci. Technol. 56 (2022) 1321–1330.

[37] C. Kuang, G. Zeng, Y. Zhou, Y. Wu, D. Li, Y. Wang, C. Li, Integrating anodic sulfate activation with cathodic $H_2O_2$ production/activation to generate the sulfate and hydroxyl radicals for the degradation of emerging organic contaminants, Water Res. 229 (2023) 119464.

[38] Y. Zong, X. Guan, J. Xu, Y. Feng, Y. Mao, L. Xu, H. Chu, D. Wu, Unraveling the overlooked involvement of high-valent cobalt-oxo species generated from the Cobalt(II)-activated peroxymonosulfate process, Environ. Sci. Technol. 54 (2020) 16231–16239.

[39] H. Song, L. Yan, J. Jiang, J. Ma, Z. Zhang, J. Zhang, P. Liu, T. Yang, Electrochemical activation of persulfates at BDD anode: Radical or nonradical oxidation? Water Res. 128 (2018) 393–401.

[40] F. Mo, C. Song, Q. Zhou, W. Xue, S. Ouyang, Q. Wang, Z. Hou, S. Wang, J. Wang, The optimized Fenton-like activity of Fe single-atom sites by Fe atomic clusters-mediated electronic configuration modulation, Proc. Natl. Acad. Sci. U.S.A. 120 (2023) e2300281120.

[41] J. Hu, Y. Li, Y. Zou, L. Lin, B. Li, X.-y Li, Transition metal single-atom embedded on N-doped carbon as a catalyst for peroxymonosulfate activation: a DFT study, Chem. Eng. J. 437 (2022) 135428.

[42] T. Zhang, H. Zhu, J.P. Croue, Production of sulfate radical from peroxymonosulfate induced by a magnetically separable $CuFe_2O_4$ spinel in water: efficiency, stability, and mechanism, Environ. Sci. Technol. 47 (2013) 2784–2791.

[43] Y. Wang, W. Qiu, X. Lu, X. Zhou, H. Zhang, X. Gong, B. Gong, J. Ma, Nitrilotriacetic acid-assisted Mn(II) activated periodate for rapid and long-lasting degradation of carbamazepine: The importance of Mn(IV)-oxo species, Water Res. 241 (2023) 120156.

[44] G. Song, H. Wu, J. Jing, X. Zhang, X. Wang, S. Li, M. Zhou, Insights into electrochemical dehalogenation by non-noble metal single-atom cobalt with high efficiency and low energy consumption, Environ. Sci. Technol. 57 (2023) 14482–14492.

[45] Z. Wu, Z. Xiong, R. Liu, C. He, Y. Liu, Z. Pan, G. Yao, B. Lai, Pivotal roles of N-doped carbon shell and hollow structure in nanoreactor with spatial confined Co species in peroxymonosulfate activation: Obstructing metal leaching and enhancing catalytic stability, J. Hazard. Mater. 427 (2022) 128204.

[46] Y. Ding, G. Zhang, X. Wang, L. Zhu, H. Tang, Chemical and photocatalytic oxidative degradation of carbamazepine by using metastable $Bi^{3+}$ self-doped $NaBiO_3$ nanosheets as a bifunctional material, Appl. Catal. B Environ. 202 (2017) 528–538.

[47] J. Hu, Y. Chen, Y. Zhou, L. Zeng, Y. Huang, S. Lan, M. Zhu, Piezo-enhanced charge carrier separation over plasmonic Au-BiOBr for piezo-photocatalytic carbamazepine removal, Appl. Catal. B Environ. 311 (2022) 121369.

[48] Y. Cheng, J. Chen, P. Wang, W. Liu, H. Che, X. Gao, B. Liu, Y. Ao, Interfacial engineering boosting the piezocatalytic performance of Z-scheme heterojunction for carbamazepine degradation: Mechanism, degradation pathway and DFT calculation, Appl. Catal. B Environ. 317 (2022) 121793.

[49] H. Yang, R. Qiu, Y. Tang, S. Ye, S. Wu, F. Qin, L. Xiang, X. Tan, G. Zeng, M. Yan, Carbonyl and defect of metal-free char trigger electron transfer and $O_2^-$ in persulfate activation for Aniline aerofloat degradation, Water Res. 231 (2023) 119659.

[50] Q. Wang, J. Lu, Y. Jiang, S. Yang, Y. Yang, Z. Wang, FeCo bimetallic metal organic framework nanosheets as peroxymonosulfate activator for selective oxidation of organic pollutants, Chem. Eng. J. 443 (2022) 136483.

[51] L. Zhang, Y. Zhang, J. Wei, W. Liu, Perovskite $LaFe_xCo_{1-x}O_{3-\lambda}$ deposited $SiO_2$ catalytic membrane for deeply cleaning wastewater, Chem. Eng. J. 403 (2021) 126386.

[52] J. Jing, X. Wang, M. Zhou, Electro-enhanced activation of peroxymonosulfate by a novel perovskite-$Ti_4O_7$ composite anode with ultra-high efficiency and low energy consumption: The generation and dominant role of singlet oxygen, Water Res. 232 (2023) 119682.

[53] A. Cabrera-Reina, M. Aliste, M.I. Polo-Lopez, S. Malato, I. Oller, Individual and combined effect of ions species and organic matter on the removal of microcontaminants by $Fe^{3+}$-EDDS/solar-light activated persulfate, Water Res. 230 (2023) 119566.

[54] F. Xiao, Z. Wang, J. Fan, T. Majima, H. Zhao, G. Zhao, Selective electrocatalytic reduction of oxygen to hydroxyl radicals via 3-electron pathway with FeCo alloy encapsulated carbon aerogel for fast and complete removing pollutants, Angew. Chem. Int. Ed. Engl. 60 (2021) 10375–10383.

[55] H. Lin, R. Xiao, R. Xie, L. Yang, C. Tang, R. Wang, J. Chen, S. Lv, Q. Huang, Defect engineering on a $Ti_4O_7$ electrode by $Ce^{3+}$ doping for the efficient electrooxidation of perfluorooctanesulfonate, Environ. Sci. Technol. 55 (2021) 2597–2607.

[56] V.K. Parida, D. Sikarwar, A. Majumder, A.K. Gupta, An assessment of hospital wastewater and biomedical waste generation, existing legislations, risk assessment, treatment processes, and scenario during COVID-19, J. Environ. Manag. 308 (2022) 114609.

[57] H. Khazri, S. Ben Hassine, I. Ghorbel–Abid, R. Kalfat, M. Trabelsi-Ayadi, Presence of carbamazepine, naproxen, and ibuprofen in wastewater from Northern Tunisia, Environ. Forensics. 20 (2019) 121–128.